University of BRISTOL

SCHOOL OF PHYSICS

FINAL YEAR PROJECT REPORT

NAME	Callum Jeffrey Brown
DEGREE COURSE	MSci Physics
PROJECT TITLE	Enhancement of negative electron affinity on the diamond (110) surface by cyclic low pressure molecular oxygen treatment and lithium deposition
YEAR OF SUBMISSION	2025
SUPERVISOR	Neil Fox and Jude Laverock
NUMBER OF WORDS	8783

Declaration

Liam Cullingford, Catherine Monk, and Ramiz Zulkharnay assisted with sample preparation in the diamond lab. Jude Laverock assisted with all experiments in the NanoESCA lab, and set up all UPS and EF-PEEM measurements. Jude, Neil Fox, and Ben Pritchard Cairns shared ideas. Ben and myself played equal parts in practical experiments. All data analysis was done by myself.

Acknowledgements

I thank Ben Pritchard Cairns for being a great project partner, and Neil Fox for his advice and guidance in the direction of the project, as well as for conceiving and making it possible in the first place. From the diamond lab I thank Liam Cullingford, Catherine Monk, and Ramiz Zulkharnay for their vital assistance with sample preparation. I also thank Ramiz for valuable discussions relating to our results, and for his patience as we fumbled our way through learning how to handle samples carefully. I thank Jude Laverock for all of the above and more: for his time and expertise using the NanoESCA, for his patience and understanding when we made mistakes, for sharing his surface science and data analysis knowledge, and for supporting our first steps into the world of scientific research.

Abstract

The termination of the (110) surface with oxygen by exposure to room temperature O_2 at pressures $\leq 1 \times 10^{-2}$ mbar is investigated by x-ray photoelectron spectroscopy (XPS). A lower concentration of oxygen is observed compared to a UV-ozone treated surface, but saturation is not reached. The O_2 treatment is used to explore the effect of repeated oxygen and lithium deposition on the electronic structure of the surface by a combination of XPS and ultraviolet photoelectron spectroscopy (UPS). A work function of 3.8 ± 0.5 eV and an electron affinity of −0.9 ± 0.6 eV are measured after deposition of approximately half a monolayer of lithium. A decrease in these quantities to 3.5 ± 0.3 eV and −1.3 ± 0.5 eV is correlated with an increase in O-Li bonding after three cycles of O_2 exposure, lithium deposition, and annealing at 500 °C. Such a decrease is not observed on an initially UV-ozone treated sample subject to the same process, which is attributed to the presence of defects.

Contents

List of abbreviations

AES	Auger emission spectroscopy
ALD	atomic layer deposition
ARPES	angle-resolved photoelectron spectroscopy
ARXPS	angle-resolved x-ray photoelectron spectroscopy
CBM	conduction band minimum
CVD	chemical vapour deposition
DFT	density functional theory
DP	diamond powder
EF-PEEM	energy filtered photoelectron emission microscopy
ESCA	electron spectroscopy for chemical analysis
FEL	fast entry lock
FOV	field of view
MWCVD	microwave-plasma chemical vapour deposition
NEA	negative electron affinity
PCD	polycrystalline diamond
PEA	positive electron affinity
RMS	root mean squared
RSF	relative sensitivity factor
SCD	single crystal diamond
SECO	secondary electron cut-off
TPD	temperature programmed desorption
UHV	ultra-high vacuum
UPS	ultraviolet photoelectron spectroscopy
UV	ultraviolet
UVO	UV-ozone
VBM	valance band maximum
XPS	x-ray photoelectron spectroscopy

1 Introduction

Efficient emission of electrons is desirable in a wide range of applications, from electron microscopy, x-ray production, and e-beam lithography, to photomultipliers, photocatalysis, and thermionic energy conversion. This is generally limited by a material's work function: the increase in electrostatic potential energy an electron initially at the Fermi level experiences if it moves to the vacuum just outside the surface, $\phi = E_{\text{vac}} - E_{\text{F}}$ [1].

In some cases, the conduction band minimum (CBM) energy of a semiconductor can be greater than the vacuum energy, so that the electron affinity, $\chi = E_{\text{vac}} - E_{\text{CBM}}$, is negative [2, 3]. In this case, conduction band electrons at the surface can be spontaneously emitted with some kinetic energy. Such negative electron affinity (NEA) is a result of the relative lowering of the vacuum energy caused by the presence of adsorbates inverting the surface dipole, as discussed in Section 2.1.

Diamond, with an ultra-wide indirect band gap of 5.47 eV at room temperature and pressure [4], is the most common material studied in this context. Its dangling carbon bonds can be terminated with a variety of species to produce an NEA, and the excellent thermal properties of diamond make it particularly suited to thermionic energy conversion devices [5]. Additionally, observations of optical phonon emission from diamond surfaces with NEA [6], alongside its compatibility with graphene, suggest possible applications in phonoelectric devices [7].

While the bare diamond surface has a positive electron affinity (PEA) of ~0.3 eV [8], synthetic diamond tends to be hydrogen terminated due to growth conditions. This results in an electron affinity of ~-1.3 eV for the (100) [9] and (111) [10] surfaces, and -1 eV for the (110) surface [11]. However, the relatively low 4 eV adsorption energy of hydrogen means these surfaces are not stable in air or at temperatures greater than 600 °C [1]. Many other terminating species have been investigated, with oxygen-metal terminations predicted to be the most stable and produce the lowest work functions and most negative electron affinities [12, 1, 13]. In an early study by Martin the oxygen-lithium terminated (100) surface was found to have a work function of (2.8 ± 0.1) eV and electron affinity of (−2.1 ± 0.1) eV [14]. O'Donnel *et al.* reported a 200 times increase in peak photoelectron emission intensity on the O-Li terminated (100) compared to the bare surface, after annealing at 800 °C [15]. A practical benefit of using lithium is that thin films are easy to deposit in vacuum by thermal evaporation.

As noted above, surface electron structure depends not only on the termination, but also on the crystal orientation. The (110) surface has only one dangling bond for each surface carbon atom, as opposed to the two of the unreconstructed (100) surface, and (110) planes grow faster than (100) planes during chemical vapour deposition (CVD), making the the surface quality more difficult to control [14]. As a result, the (110) surface has not been studied as much as the (100) and (111) surfaces. To the author's knowledge, this is the first study of oxygen-lithium termination of the (110) diamond surface.

This work builds on that of Greenwood, who recently demonstrated the use of room temperature O_2 exposure at 1.5 bar for the purposes of oxygen-lithium termination, and measured electron affinities of (−1.7 ± 0.2) eV and (−1.5 ± 0.3) eV for the (100) and (111) diamond surfaces respectively [16]. This oxygen treatment can be easily carried out in the University of Bristol NanoESCA facility without breaking vacuum, and is less aggressive than methods involving atomic oxygen, which can roughen the surface [17] . A variety of methods that have been used for oxygen termination in the literature are reviewed in Section 3.

By conducting oxygen termination in the same vacuum system as lithium deposition, the ability to apply multiple cycles of the treatment is enabled. This type of repeated treatment is routinely used with caesium and oxygen for production of gallium based NEA photocathodes, where it is called the yo-yo method [18, 19].

Here, the use of low O_2 pressures of $\lessapprox 1 \times 10^{-2}$ mbar for terminating the bare (110) diamond surface is investigated by XPS. These lower pressures are more economical in terms of oxygen use, and more convenient in high vacuum systems. Then, a yo-yo process of repeated oxygen

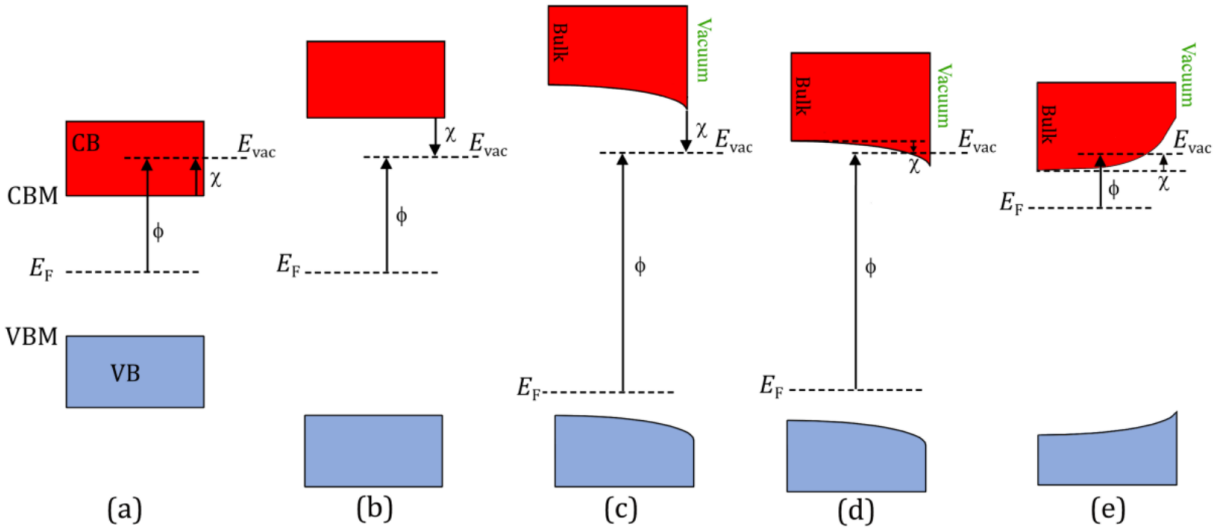

Figure 1: Band structure diagrams of semiconductors with: (a) PEA, (b) true NEA, (c) true NEA despite downward band bending at the surface, (d) effective NEA as a result of downward band bending at the surface, and (e) PEA where the CBM is above the vacuum level at the surface. Reproduced from Ref. [1].

exposure, lithium deposition, and 500 °C stabilising anneal is explored by a combination of XPS and ultraviolet photoelectron spectroscopy (UPS). A UV-ozone (UVO) treated surface is used as a comparative initial oxygen termination.

2 Theory

2.1 Negative electron affinity

The relative energy difference between the CBM of a semiconductor and the vacuum level, called the electron affinity, χ, is affected by the dipole at the surface of the material. Primary causes of this dipole are the presence of surface states with energies in the band gap, which also cause fermi level pinning, and adsorbates [20]. By choosing an adsorbate that is more electropositive than the bulk atom, a dipole with the positive side pointing away from the surface can be formed. If the CBM energy is sufficiently high, as in wide bandgap semiconductors, this can bring the vacuum level below the CBM, so that a negative electron affinity (NEA) is formed [1].

Band bending at the surface, which can be caused by doping, surface states, and adsorbates, leads to a distinction between so-called true and effective NEA, as shown in Figure 1. If the CBM at the surface lies above the vacuum level despite downward band bending, the NEA is true. Effective NEA, on the other hand, occurs when the CBM lies above the vacuum level in the bulk, but is brought below by downward band bending leading to a PEA at the surface.

More comprehensive introductions to NEA can be found in Refs. [21, 1].

If the difference in energy between the Fermi level and the valance band maximum (VBM), $E_F - E_{VBM}$, the work function, ϕ, and the band gap, E_g, are known, the electron affinity can be calculated:

$$\chi = (E_F - E_{VBM}) + \phi - E_g \,. \tag{1}$$

The band gap is a bulk parameter which does not change with surface termination, so literature values can be used. The other two parameters can be measured using UPS as discussed in Section 2.2.2.

2.2 Photoelectron spectroscopy

Photoelectron spectroscopy involves exposing a material to electromagnetic radiation and measuring the kinetic energy spectrum of electrons emitted as a result of having absorbed the energy of a photon. As the mean free path of the escaping electrons is on the order of 1-10 nm (depending on the photon energy), photoelectron spectroscopy is highly surface sensitive.

The electron spectrum is most commonly measured by a concentric hemispherical analyser, in which a voltage applied across an inner and outer hemisphere causes the path of an electron moving in the analyser to bend towards the inner hemisphere. The voltage can be tuned to allow only electrons with a narrow range of kinetic energies to reach the detector: the paths of slower electrons are bent more and they hit the inner hemisphere, while the paths of faster electrons are bent less and they hit the outer hemisphere. A schematic of such a system is shown in Figure 2(a).

The energy spectrum is often presented on a binding energy scale with respect to the sample Fermi level, where the measured kinetic energy and the work function of the spectrometer is subtracted from the photon energy to give the minimum energy required to emit an electron with that kinetic energy. Inelastic scattering within the material leads to the emission of "secondary electrons" with lower kinetic energy. These appear on the high binding energy side of the feature they originated from. The angle of the analyser with respect to the sample normal influences the surface sensitivity: at greater angles, electrons travelling towards the analyser must travel further to reach the surface, and so are more likely to be inelastically scattered.

The photon energy used broadly determines what structure can be measured. This splits photoelectron spectroscopy into two main classes: x-ray photoelectron spectroscopy (XPS) and ultraviolet photoelectron spectroscopy (UPS).

2.2.1 X-ray photoelectron spectroscopy

Soft x-rays with photon energies on the order of 1 keV probe the core atomic levels of atoms in the top ~10 nm of a sample. An illustration of x-ray photoelectron emission from a 1s core level is shown in Figure 2(b). The binding energy of core level electrons is characteristic of the element and its bonding environment, enabling determination of the near surface chemistry of a sample. In this sense XPS is also known as electron spectroscopy for chemical analysis (ESCA).

An example of a low resolution survey spectrum of the UVO treated sample used in this work is shown in Figure 3. The oxygen 1s (O 1s) photoelectron peak is visible at a binding energy ~532 eV atop the secondary electron background from the intense carbon 1s (C 1s) peak at ~284 eV. Also labelled, but not discussed here, are the carbon and oxygen KLL Auger peaks at high binding energy, and the valance band (VB) structure near the Fermi level (zero binding energy),

The area beneath a photoelectron peak is proportional to the number concentration of atoms contributing to the signal. The atomic percentage (at%) of element X can be calculated by:

$$\text{X at\%} = \frac{I_X}{\text{RSF}_X} \div \sum_Y \frac{I_Y}{\text{RSF}_Y}, \tag{2}$$

where I_X is the area of peak X above the background, RSF_X is the relative sensitvity factor of the instrument for that peak, and Y are the other elements observed by XPS. The relative sensitivity factor (RSF) is required because lighter elements emit fewer photoelectrons per atom than heavier elements, and the response of the instrument will vary depending on the energy analysed. It is important to note that, due to the surface sensitivity of the technique, atoms nearer to the surface contribute more to the observed signal than those further below. Thus, an atomic percentage of say 5 at% calculated by Equation 2 does not necessarily indicate that 5% of the atoms in the near surface region are of that element. More absolute calculations

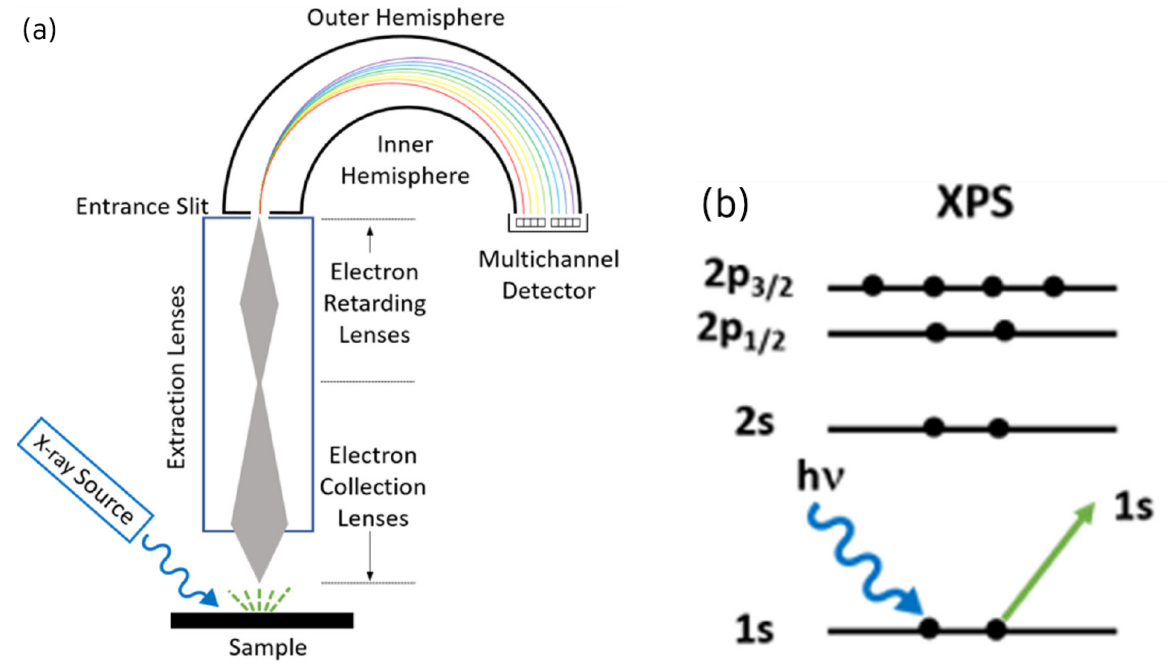

Figure 2: (a) A schematic of an XPS instrument at normal emission angle showing a concentric hemispherical analyser. (b) An illustration of photoelectron emission from the 1s core level. Both figures are reproduced from Ref. [22].

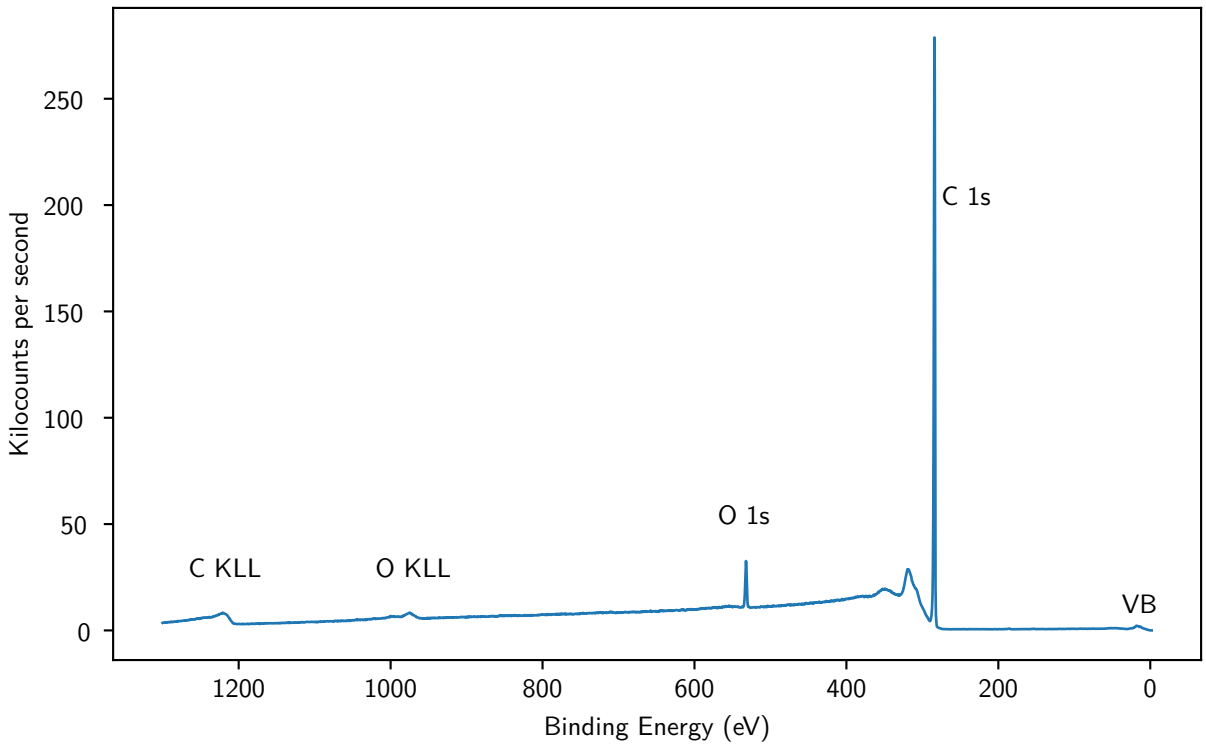

Figure 3: XPS survey spectrum of the UVO treated (110) sample with the main features labelled.

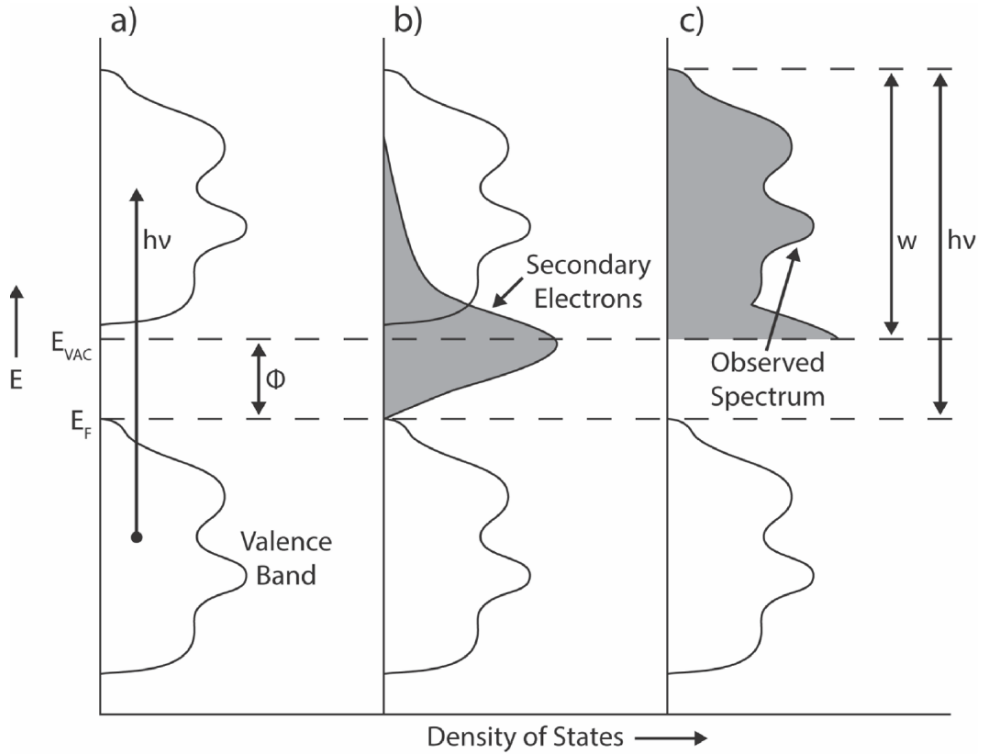

Figure 4: Illustration of the formation of a UPS spectrum. (a) Excitation of electrons from the valance band to above the vacuum level in the bulk material. (b) Formation of a secondary electron distribution as the excited electrons move towards the surface. (c) Electrons with less than the vacuum energy cannot escape the surface and are not observed. Reproduced from Ref. [23].

of the relative abundance of elements at the surface can be done, but they are complex and can require many assumptions, so are not attempted here.

Quantitative information about how an element is bonded can be extracted by fitting its photoelectron peak to a model — usually the sum of multiple peak-like line shapes and a representation of the background signal. For example carbon-oxygen bonds are generally seen at higher binding energy than carbon-carbon bonds [17]. Such analysis is not conducted in this report.

The physics of XPS and the interpretation of the acquired spectra are considerably more complicated than presented here. A more complete introduction is given by Ref. [22].

2.2.2 Ultraviolet photoelectron spectroscopy

Deep ultraviolet (UV) photons with energies on the order of tens of eV probe the valence band rather than core atomic levels. UPS is even more surface sensitive than XPS as the energy of excited electrons is closer to the minimum of the universal inelastic mean free path curve, such that almost all those that escape are from the top 1-2 nm [23].

The general process of emission from a metal is illustrated in Figure 4. UV light with photon energy $h\nu$ excites electrons from below the Fermi level to energies greater than the vacuum level. Inelastic scattering as the excited electrons travel towards the surface results in the formation of a secondary electron distribution which is independent of the valence band structure. At the surface, only electrons with energy greater than the vacuum level can escape, and so the secondary electron distribution is cut off.

The kinetic energy of the escaped electrons is measured with respect to the Fermi level of the detector, which is the same as the Fermi level of the sample due to the sample and detector

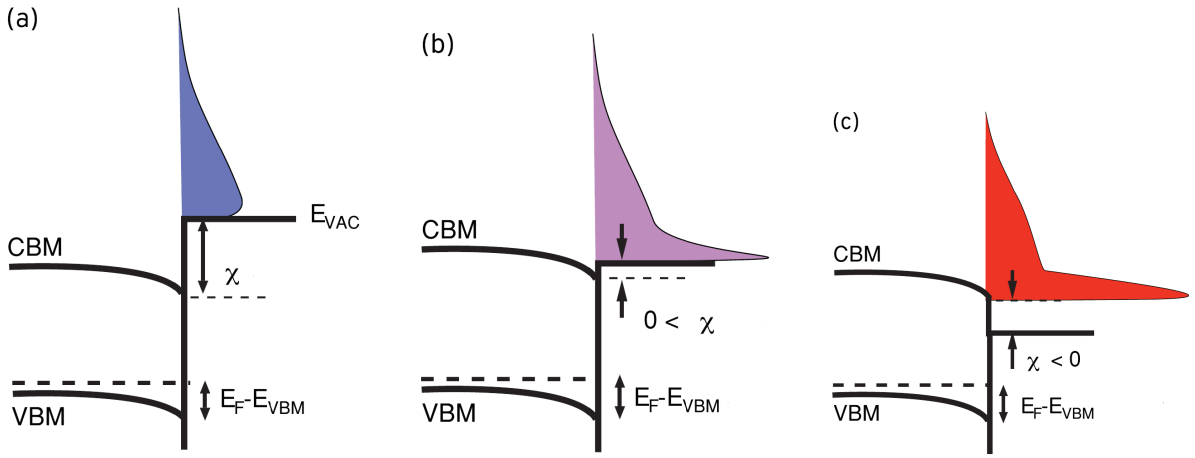

Figure 5: Illustrations of the general form of secondary electron spectra expected from semiconductors with (a) PEA, (b) effective NEA, and (c) true NEA. Adapted from Ref. [15].

being electrically connected. In order to detect the low kinetic energy electrons which could only just escape, and so measure the energy of the vacuum level with respect to the Fermi level (the work function), a voltage V_{bias} is used to accelerate the emitted electrons.

Therefore, the binding energy E_{B} of an electron with measured kinetic energy E_{K} is:

$$E_{\text{B}} = h\nu - E_{\text{K}} - eV_{\text{bias}}\,, \tag{3}$$

where both E_{B} and E_{K} are relative to the Fermi level E_{F}. The work function of the sample can then be calculated from the binding energy of the secondary electron cut-off (SECO) [23]:

$$\phi = h\nu - E_{\text{B, SECO}}\,. \tag{4}$$

The energy gap between the Fermi level and the VBM in a semiconductor results in a cut off on the low binding energy side of the spectrum at the VBM energy [5], and so the electron affinity can be calculated using Equation 1.

As band bending extends much further into the bulk than the information depth of UPS [24], the calculated electron affinity will be that at the surface. Therefore effective NEA materials with downward band bending will be measured to have a PEA. Figure 5 illustrates the effect of electron affinity on the observed secondary electron peak. In a semiconductor, the maximum of the secondary electron distribution occurs in the region of the CBM. Therefore, in PEA materials only the tail is observed, whereas in NEA materials an intense peak is measured. Figure 5(c) assumes that no secondary electrons have energies within the bulk bandgap, whereas in reality, surface and defect states can allow scattering to energies below the CBM. For the purposes of this work it is assumed that the secondary electron distribution is cut off at the vacuum level, allowing true NEA to be measured by UPS, but this is debated [15, 25].

A more holistic introduction to UPS is given by Ref. [23].

3 Review of oxygen termination of diamond

To produce a consistent NEA by oxygen-metal termination, a uniform layer of chemically bonded oxygen is required. However, the oxidation is difficult to control due to defects in the surface (roughness, contamination, etc.) and the complex chemistry involved.

Oxygen can bond to the diamond surface in ketone (C = O) and bridging ether (C – O – C) functional groups, as well as hydroxy (C – OH) and other groups with a C – O bond if there are other species present. The relative proportions of these bonds depend on the oxidation method

[17] and the crystal orientation of the surface [26], and impacts subsequent metal adsorption. For example, it has been calculated using density functional theory (DFT) that on the (100) surface scandium adsorbs preferentially on ketone sites [13]. Complicating comparison with theoretical calculations, which use atomically flat diamond surfaces, is the formation of an sp^2 hybridised graphitic or amorphous carbon layer during oxidation [17, 27].

Experimental characterisation of oxygenated surfaces produced by a variety of methods is, therefore, important in understanding how oxygen impacts NEA and stability after metal deposition. A host of techniques including temperature programmed desorption (TPD) and variations on electron spectroscopy, diffraction, and microscopy are used for this purpose. Most commonly, XPS is used to determine the atomic concentration of carbon and oxygen, and the relative abundance of their various bonding arrangements, in the near surface region. Assuming all detected carbon is sp^3 , Vidrio *et al.* calculated that an atomic concentration of oxygen of ~6 at% corresponds to 1 monolayer coverage on a (100) surface, however this does not translate directly to real situations due to the presence of sp^2 carbon [28].

3.1 Approaches

There are a number of ways to oxidise diamond surfaces, the most common of which will be discussed here. A comparison table can be found in Appendix A.

Acid oxidation involves submerging the surface in a hot acid mixture, for example H_2SO_4 and HNO_3, generally for an hour or more, followed by rinsing in deionised water and drying. Oxygen concentrations of between about 5 and 15 at% (measured by XPS) have been reported for various mixtures and processes on the (100) surface, with C – OH being the majority bond type [17, 27, 28, 29, 30].

In **UV-ozone** treatment, UV light causes the formation of atomic oxygen (O) by the dissociation of O_2 and O_3 (which is formed by the reaction of O and O_2). Atomic oxygen reacts with the diamond surface, displacing existing C – H bonds [5]. Saturation of the oxygen concentration at between 5 and 8 at% on the (100) surface can be achieved in around 30 minutes by commercial UV-ozone cleaners, in which the O_2 may be present in ambient air, or flowed through a chamber, possibly with a substrate heater [17, 28, 16]. Navas *et al.* reported that a room temperature low pressure (500 mbar) treatment for 2 hours in a vacuum chamber produced a slightly lower atomic concentration of oxygen (5.5 at%) than an atmospheric pressure treatment at 80 °C for 20 minutes (6.8 at%) [29].

Thermal cracking of O_2 at 2×10^{-6} mbar into a mix of O and thermally excited O_2* by a heated filament in vacuum has been reported by Wan *et al.* to result in unsaturated O 1s to C 1s area ratios (scaled by sensitivity factors) of 7% for (100) and 7.5% for (111) surfaces after 130 minutes [31]. It was suggested that saturation was not reached due to roughening of the surface by high energy atomic oxygen providing additional surface area. However, this was not reproduced by Zulkharnay *et al.*, who found only 4.3 at% oxygen using the same conditions and determined that bridging ether C – O – C bonds were the large majority [17].

TPD experiments have suggested that **O_2 exposure** in a vacuum chamber at room temperature is ineffective on both the hydrogenated (100) [32] and unterminated (110) [33] surfaces, although in both cases exposure dosage was not given. The same papers reported that thermally excited **O_2*** (produced by a hot filament assumed not to cause cracking) led to saturation after 7×10^5 Langmuir (L), and 2.4×10^3 L respectively. In contrast, TPD experiments on unterminated (111) and (110) surfaces by Bobrov *et al.* showed changes in the CO desorption peaks below 144 L of room temperature exposure [34]. Dontschuk *et al.* conducted an O_2 exposure scan from 1 L to 1×10^5 L on a (100) surface which was confirmed to be hydrogen free by observation of a surface reconstruction peak in the XPS C 1s spectrum. They observed saturation after 1×10^4 L, and stability at 450 °C, but 60% desorption at 750 °C. Greenwood reported that exposure to a very high dosage of 1.3×10^{12} L (1.5 bar for 20 minutes) produced an oxygen concentration of 3.7 at% on the (100) surface and 1.5 at% on the (111) surface (both

Table 1: Reactor conditions for MWCVD growth of boron-doped diamond on a single crystal (110) substrate.

Duration	45 min
Power	1 kW
Pressure	100 Torr
H_2	300 sccm
CH_4	12.5 sccm
B_2H_6	0.5 sccm
Emissivity	0.13
Temperature	~860 °C

assumed previously unterminated) [16]. In light of these disagreements, further exploration of O_2 exposure as a method of oxygenating the diamond surface is needed.

4 Methods

4.1 Sample preparation

A 6.8×3.3 mm, CVD grown, (110)-orientated single crystal diamond (SCD) substrate manufactured by Element Six was acid cleaned to remove polishing residue following the procedure in Ref. [5]. Details of the substrates are given in Appendix B. To avoid charging during electron spectroscopy measurements, a conductive boron-doped diamond layer was grown using microwave-plasma chemical vapour deposition (MWCVD). The sample was mounted on a Molybdenum disk which was held 0.5 mm above the water cooled base plate of a reactor with the same design as that detailed in Ref. [35]. The conditions used are given in Table 1.

Raman spectroscopy did not show signs of boron, indicating that the doping was low. The root mean squared (RMS) roughness over a 130×130 mm^2 area was 12 nm as measured using an Olympus LEXT OLS5100 confocal laser microscope. The sample was laser cut into two approximately 3×3 mm pieces.

Prior to measurements, the samples were hydrogen terminated by plasma treatment following the procedure in Ref. [5]: cleaning at ~900 °C / 140 Torr, terminating at ~550 °C / 50 Torr, and cooling at 30 Torr, for two minutes each. The short duration is thought not to result in the formation of (111) microfacets on the (110) surface as has been reported for longer treatments [36]. One sample was then oxygen terminated by a Jelight model 42 UV-ozone cleaner for 30 minutes. From now on the samples are denoted (110)-H and (110)-O for the hydrogen terminated and UV-ozone treated samples, respectively.

The samples were loaded into the University of Bristol NanoESCA Facility vacuum system in molybdenum sample holders without adhesive, and annealed at 300 °C for one hour to desorb atmospheric contaminants physisorbed to the surface. The (110)-H sample was further annealed for 1 hour at 900 °C to desorb the hydrogen termination. Heating was provided by a resistive filament below the sample holder, for which the temperature had previously been calibrated to the filament current.

4.2 X-ray photoelectron spectroscopy measurements

After each processing step, XPS measurements were taken using a monochromatic Al Kα x-ray source with a photon energy of 1486.7 eV, and a hemispherical ScientaOmicron Argus analyser at an angle of 35° to the sample normal. The small size of the samples necessitated use of a collection aperture (A4) with good spatial definition, but which produces asymmetric line-shapes. Survey scans were taken in 0.5 eV steps with a 50 eV pass energy, while all other scans used

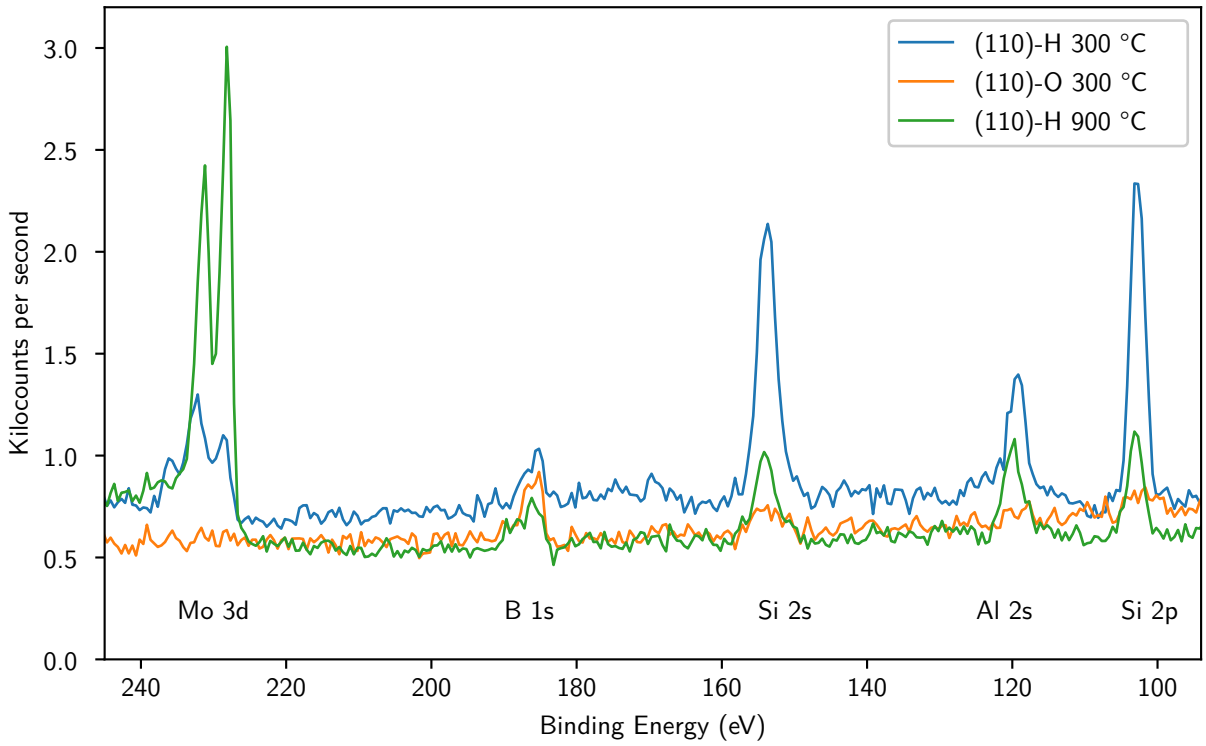

Figure 6: XPS survey spectra showing contaminants on the (110)-H surface prior to the low pressure molecular oxygen treatment experiments.

0.05 eV steps and a pass energy of 20 eV. The pressure in the NanoESCA preparation chamber during measurements was between 1×10^{-10} and 1×10^{-9} mbar. No charging was observed, indicating that the samples were sufficiently doped.

4.3 Evaluation of surface cleanliness

XPS survey spectra showed the (110)-O sample to be clean and oxygen terminated. The (110)-H sample, however, was contaminated with molybdenum, silicon, and aluminium, as shown in Figure 6, and oxygen (see Section 5.2). The silicon and aluminium were identified as originating from oxides.

The molybdenum, with a very high melting point of 2623 °C, is an unusual contaminant, and the 900 °C anneal led to an increase in the observed signal. Use of a collection aperture (A2), with a narrower field of view than aperture A4, verified that the molybdenum originated from the sample rather than the sample holder. It is attributed to molybdenum carbide which was incorporated into the diamond bulk during the growth process, and diffused towards the surface during annealing.

The 900 °C anneal reduced, but did not remove the other contaminants, indicating some presence in the bulk diamond. Subsequent survey spectra indicated that the concentration of these contaminants remained approximately constant throughout processing, and so for practical reasons they are neglected for the purpose of quantitative analysis. Therefore, atomic concentrations calculated for the (110)-H sample must not be treated as absolute, but should retain approximate relative meaning.

4.4 Low pressure molecular oxygen treatment

After the 900 °C anneal, the (110)-H sample was exposed to molecular oxygen (O_2) for various times at various pressures in the NanoESCA fast entry lock. The pressure was set through balancing the inflow through a leak valve with pumping from a turbo pump.

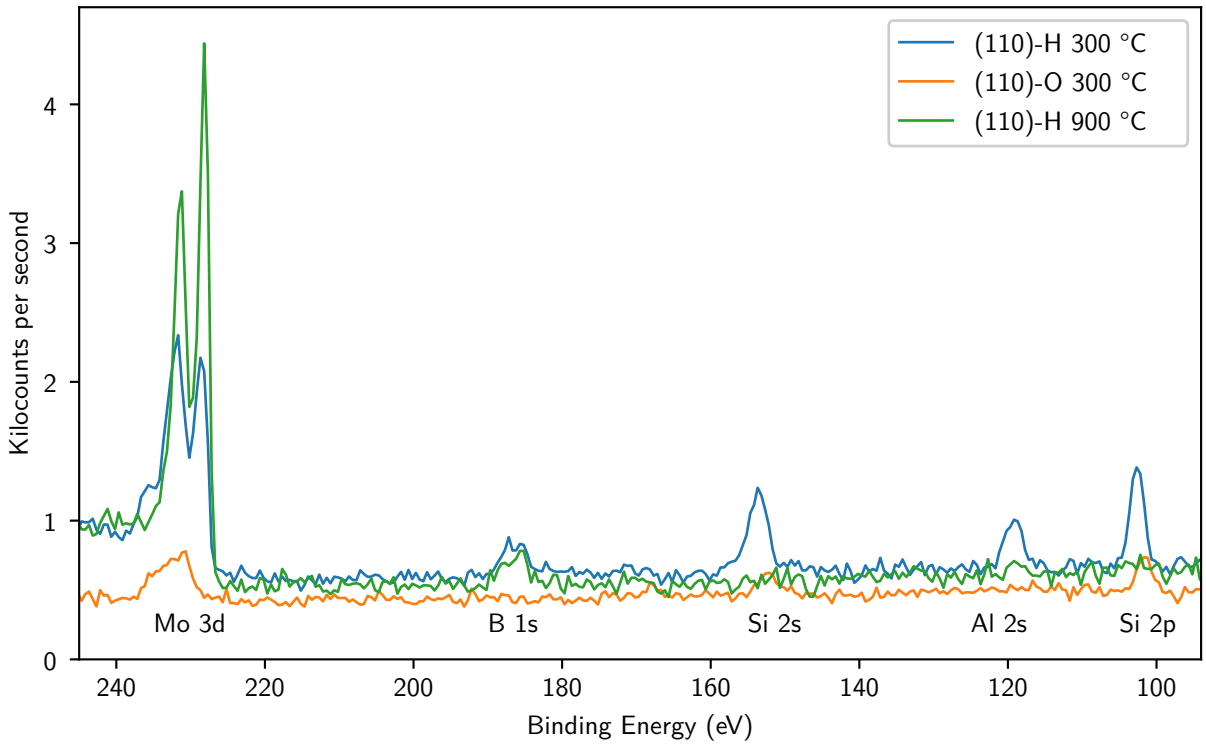

Figure 7: XPS survey spectra showing contaminants prior to the oxygen-lithium yo-yo process experiments.

First, a "pressure scan" from 1×10^{-6} mbar to 1×10^{-3} mbar in orders of magnitude was completed, with 5 minutes exposure at each step. The average background pressure before introduction of O_2 was 5.0×10^{-8} mbar.

Next, the surface was "reset" by a 900 °C anneal then exposed to approximately 1×10^{-2} mbar O_2 for 1, 5, and 13 minutes in succession at a background pressure of 6.7×10^{-8} mbar. This is referred to as the "time scan".

Following this, the sample was annealed at 300 °C then 500 °C, with a 5 minute exposure at ~1×10^{-3} mbar (~3×10^{5} Langmuir) after each. Finally, the sample was exposed for an additional 5 minutes at ~1×10^{-2} mbar (~4.6×10^{6} Langmuir).

The cumulative exposure in Langmuir was calculated by numerically integrating the pressure, which was recorded at 1 second intervals, after subtracting the background pressure. The pressure gauge used, which was calibrated primarily for ultra-high vacuum (UHV) operation was later found to read $(1.0 \pm 0.1) \times 10^{-3}$ mbar lower than a Pirani gauge calibrated for higher pressures when tested at ~1×10^{-2} mbar. A -1×10^{-3} mbar correction was applied for exposures at ~1×10^{-2} mbar, and the higher pressure gauge was used for subsequent O_2 exposures.

4.5 Retermination

Prior to further experiments, both samples were re-hydrogen terminated, and the (110)-O sample was again UV-ozone treated. The samples were cleaned by annealing for 1 hour at 300 °C, then the (110)-H sample was annealed at 900 °C for a total of 1 hour and 45 minutes to desorb the hydrogen.

As shown in Figure 7, the (110)-H sample was again contaminated with silicon and aluminium oxides, which were almost eliminated by the high temperature anneal, and molybdenum, which behaved as discussed in Section 4.3. The Mo 3d peak was also observed on XPS survey spectra of the (110)-O sample, however the use of aperture A2 confirmed this originated from the sample holder rather than the sample. Due to a higher binding energy, it was identified as mo-

lybdenum oxide rather than molybdenum carbide [37]. The contribution of this oxide to the O 1s peak was neglected, and hence oxygen atomic concentrations calculated for the (110)-O sample for the yo-yo experiments should be treated as approximate.

4.6 Oxygen-lithium yo-yo process

After retermination and annealing at 900 °C, the (110)-H sample was exposed to ~1×10^{-2} mbar of O_2 for 10 minutes (~4.5×10^6 Langmuir). Subsequent steps were performed on both samples, except where noted.

Fourteen days later, another 300 °C cleaning anneal was done prior to lithium deposition by thermal evaporation for 152 seconds, corresponding to approximately half a monolayer. The background pressure in the NanoESCA deposition chamber prior to deposition was in the low 10^{-9} mbar range and the lithium source was at ~445 °C. To investigate the thermal stability of the surface, the samples were annealed for 45 minutes at 300 °C and 500 °C in succession.

Eight days later, a cleaning anneal was performed preceding a second and third cycle of: ~4.5×10^6 Langmuir of O_2 exposure, 152 seconds lithium deposition, and a 45 minute 500 °C anneal. The (110)-H sample was also subjected to a fourth cycle.

Small amounts of fluorine contamination were occasionally observed on XPS survey spectra after lithium deposition as in Ref. [16], which used the same equipment. The presence of fluorine was neglected for the purpose of quantitative analysis.

4.7 Ultraviolet photoelectron spectroscopy and energy filtered photoelectron emission microscopy measurements

For the lithium experiments, the work function and VBM at each step was determined by UPS, and energy filtered photoelectron emission microscopy (EF-PEEM) was used to produce real space work function maps for the first deposition/annealing cycle. Measurements were taken using a ScientaOmicron NanoESCA II at normal emission angle with a He I excitation source (photon energy 21.22 eV). A high emission current observed from the (110)-O necessitated the use of a lower 5 kV extraction voltage compared to the normal 12 kV, which was used for the (110)-H sample. This could have been due to field enhancement from the high density of defects observed on the surface, edge effects from the small window of the sample holder, or a number of other reasons. It led to a larger field of view (FOV) for EF-PEEM measurements of ~160 µm compared to ~120 µm for 12 kV operation, but did not significantly affect energy or spatial resolution.

Effort was made to measure the same representative area of the samples each time. When this was not possible, another representative area was chosen. Notably, the area of the (110)-O sample measured after the first 300 °C cleaning anneal contained visually different defects than that measured after subsequent steps.

For EF-PEEM measurements a 150 µm contrast aperture was used to improve spatial resolution. Image data at each step of 25 meV in a 1-2 eV range around the work function was collated to produce the low kinetic energy part of the UPS spectrum at each pixel. The work function at each pixel was extracted by extrapolating the maximum gradient of the low kinetic energy edge to the background, which was approximated as the minimum detected intensity.

For UPS measurements an iris was used to reduce the maximum counts per second to a safe level for the Channeltron detector, leading to a smaller analysis area than for EF-PEEM. Data was taken in 25 meV steps from 20 to −1 eV binding energy, and normalised to the “knee” near 8 eV binding energy as described in Refs. [6, 5].

The SECO was determined by fitting a straight line to the six data points centred on the change of sign of the second derivative of intensity, and finding its intercept with the binding energy axis (the background was negligible). The work function was then calculated using Equation 4. The uncertainty was calculated by propagation of the uncertainties in the fitted slope and intercept. Similarly, the VBM energy relative to the Fermi level was determined by

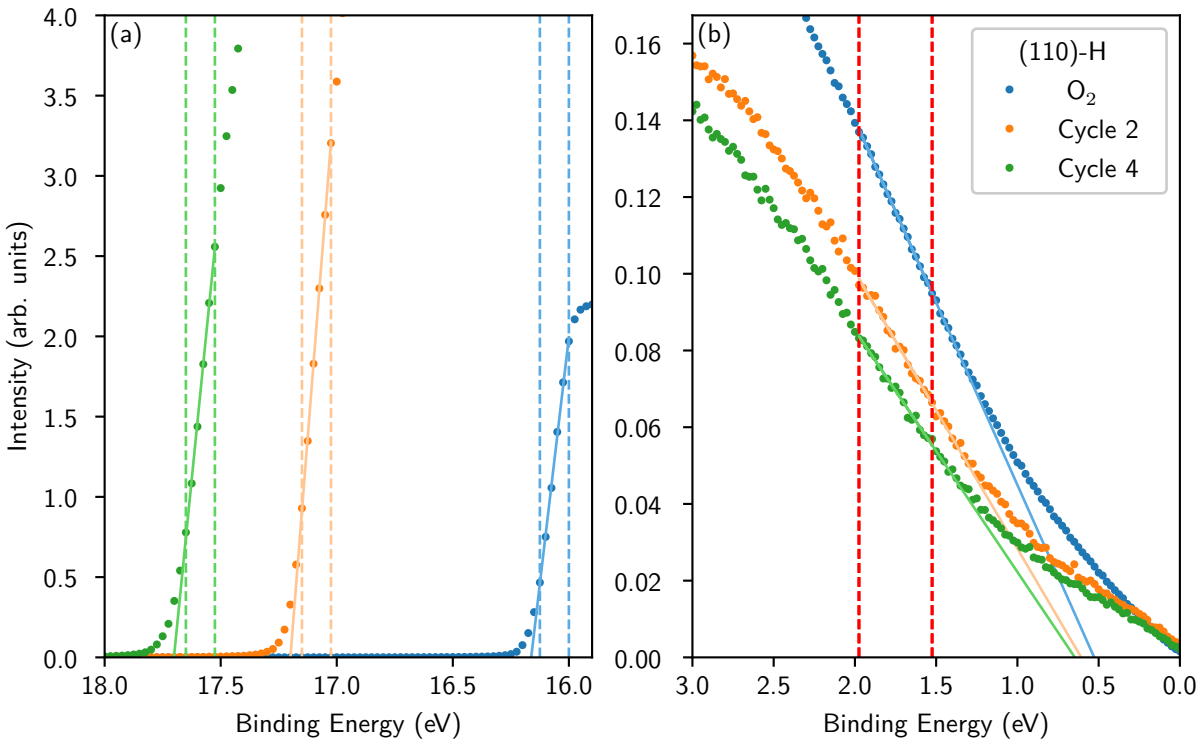

Figure 8: Examples of the range selection and linear fits used for determination of (a) the SECO and (b) the VBM for the (110)-H sample at selected processing steps. The dashed lines indicate the range used for fitting.

the intercept of the binding energy axis with a linear fit to the 1.5-2.0 eV range. The choice of range use to determine the VBM energy can be somewhat arbitrary, as noted by Grabowski *et al.* [38]. This range was chosen as it was visually linear for all spectra, providing some consistency in lieu of a more rigorous range-choosing method. Representative examples of the linear fits used for SECO and VBM determination are shown in Figure 8.

4.8 Quantitative XPS

To quantify the relative amounts of oxygen, carbon and lithium detected by XPS, the areas of the O 1s, C 1s and Li 1s peaks above the background were numerically integrated after correction for the instrument transmission function. Atomic concentrations were calculated using Equation 2 with relative sensitivity factors of 1, 2.93, and 0.0568 for C 1s, O 1s, and Li 1s respectively.

For O 1s peaks, a linear background was fitted to the region outside the peak, as shown in Figure 9(a). For C 1s peaks a static iterative Shirley background was calculated between 280 and 290 eV using lmfitxps [39], as shown in Figure 9(b).

The very low RSF of the Li 1s peak led to noisy data for a total dwell time of 3 seconds per 0.05 eV step. In addition, the background signal around the peak was non-linear. Therefore the area was found by fitting a model, consisting of the sum of a Voigt peak with a 4 knot cubic spline background, and calculating the area under the fitted curve. Examples of this fit for the (110)-H sample after the first lithium deposition and after the fourth cycle are shown in Figure 10. The better statistics resulting from an overnight measurement after the fourth cycle, with a total dwell of 103 seconds per step for the Li 1s spectrum, allow the shape of the background to be seen more clearly.

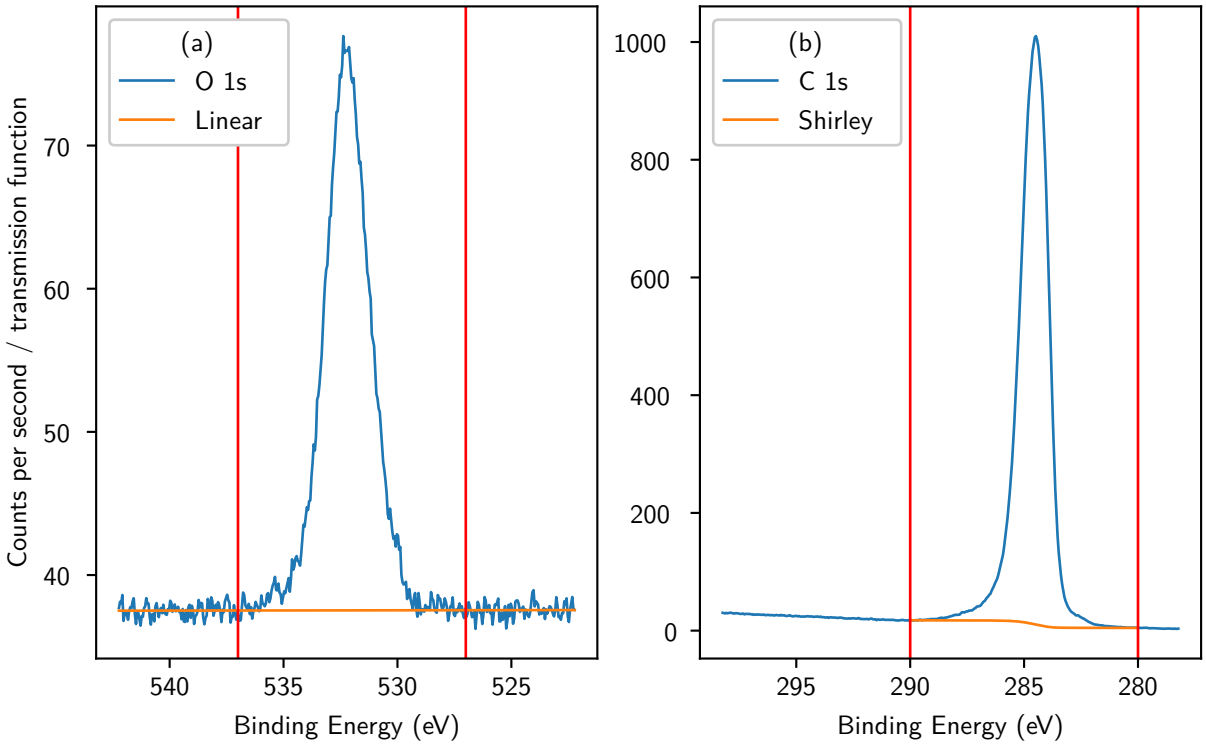

Figure 9: Examples of (a) a linear background fitted to the region outside the O 1s peak, and (b) an iterative Shirley background calculated for the C 1s peak. The chosen peak limits are indicated by the vertical red lines.

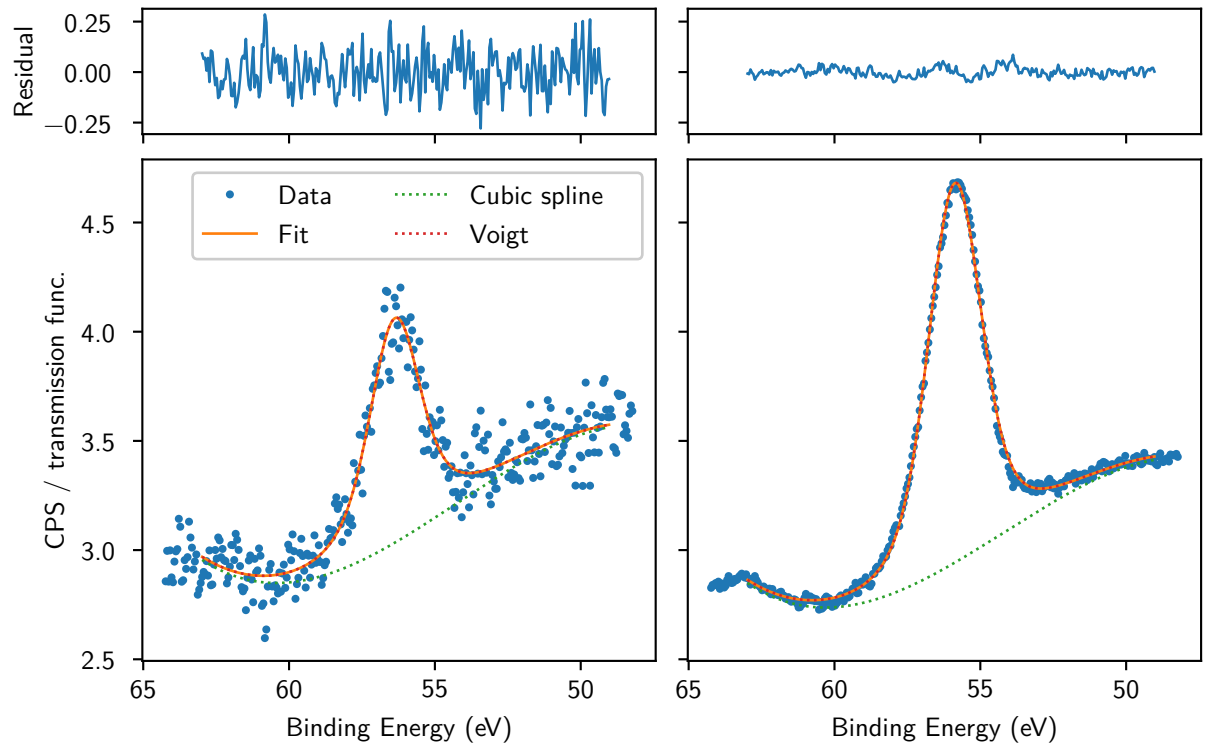

Figure 10: Examples of fits to the Li 1s peak of the (110)-H sample after the first lithium deposition (left), and after the fourth cycle (right).

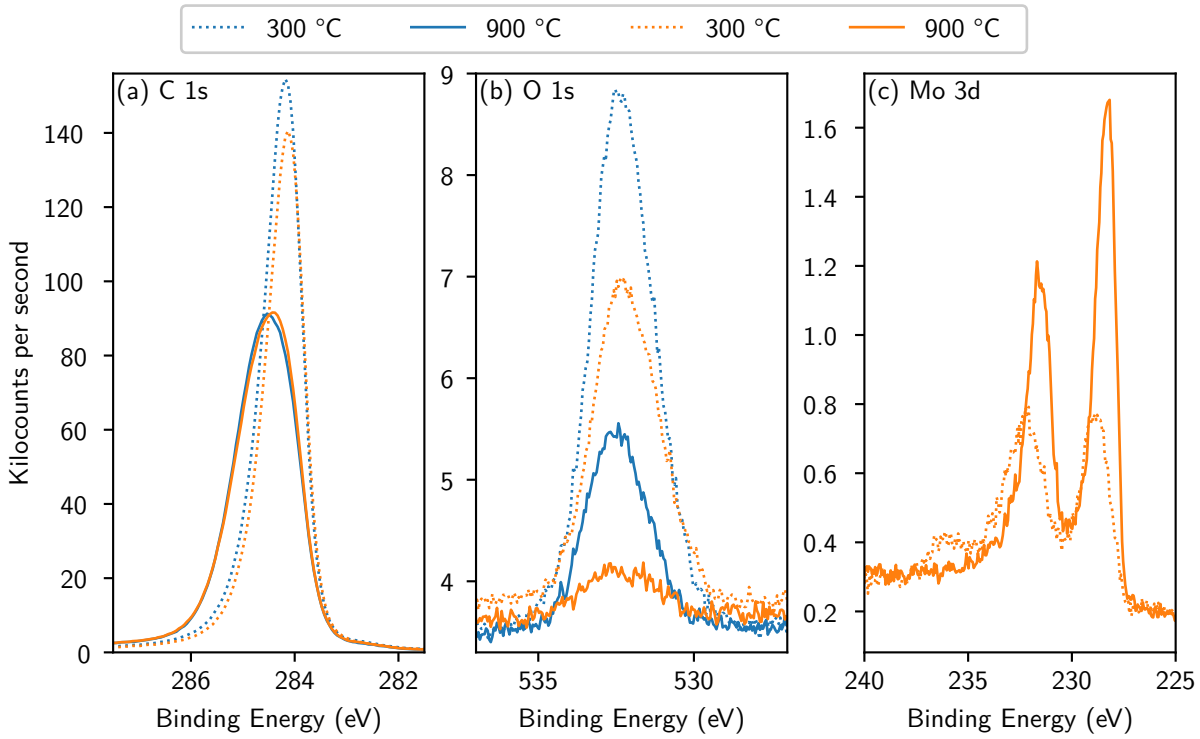

Figure 11: (a) Broadening and shift of the C 1s peak ~0.3 eV to higher binding energy after annealing the hydrogen terminated (110)-H sample at 900 °C. The blue and orange lines indicate the first and second times the sample was hydrogen terminated, respectively. (b) No such change in the O 1s peak. (c) Increase in the Mo 3d peak.

Table 2: Atomic concentrations before and after the second 900 °C hydrogen desorption anneal, when neglecting or accounting for molybdenum.

	Step	C 1s (at%)	O 1s (at%)	Mo 3d (at%)
Neglecting Mo	300 °C	98.2	1.8	N/A
	900 °C	99.7	0.3	N/A
Including Mo	300 °C	98.0	1.8	0.2
	900 °C	99.3	0.3	0.3

5 Results

5.1 Hydrogen desorption anneals

Annealing the (110)-H sample at 900 °C after it had been hydrogen terminated caused the C 1s peak to broaden and the maximum to shift by ~0.3 eV to higher binding energy, as shown in Figure 11. After the first such anneal (before the low pressure O_2 scans) the area of the C 1s peak decreased by 13%, while after the second (before the yo-yo experiment), the decrease in area was only 2%. Both anneals caused the oxygen contamination to decrease by 1.5 at% to 1.1 and 0.3 at% respectively, but no shift or broadening was observed in the O 1s peak.

A dedicated Mo 3d scan was conducted before and after the second hydrogen desorption anneal, showing an increase in area of 32%, but little change in atomic concentration, as displayed in Table 2. The shift of the Mo 3d spectrum to lower binding energy seen in Figure 11(c) is attributed to the loss of molybdenum oxides observed at a binding energy of ~236 eV prior the desorption anneal.

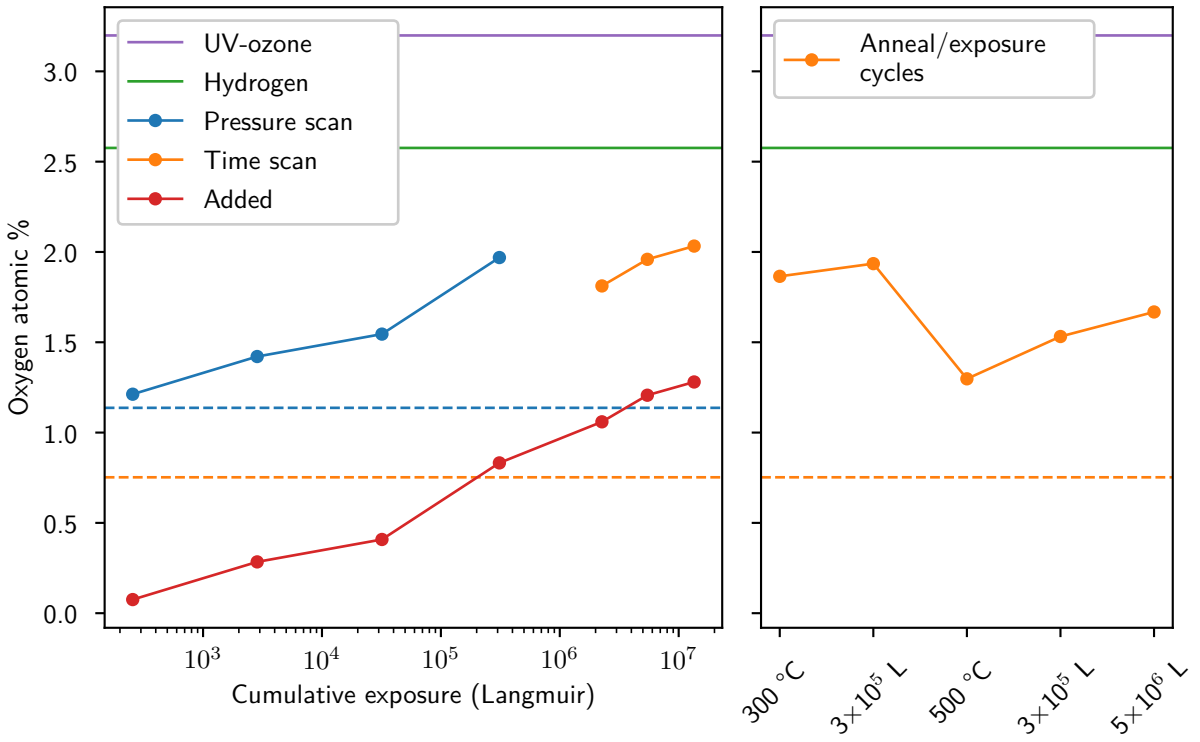

Figure 12: Approximate oxygen atomic concentration against the logarithm of cumulative O_2 exposure in Langmuir for the two exposure scans, and the repeat anneal/exposure cycles on the (110)-H sample. Concentrations for the (110)-O sample (3.2 at%, purple) and the (110)-H after 300 °C but before 900 °C anneals (2.6 at%, green) are given as reference. The background concentrations after a 900 °C anneal before the pressure scan (1.1 at%, blue) and the time scan (0.8 at%, orange) are shown as dashed lines. The oxygen content added above the background for both scans is plotted in red. Lines connecting data points serve only to guide the eye.

5.2 Low pressure molecular oxygen treatment

During the pressure scan, the oxygen concentration increased to a maximum of 2.0 at% after the 1×10^{-3} mbar exposure. This corresponded to an addition of 0.9 at% above the background contamination of 1.1 at%. In comparison, the UVO treated sample showed a concentration of 3.2 at%.

After the surface was reset by a 900 °C anneal, the background contamination decreased to 0.8 at%. The time scan at 1×10^{-2} mbar then added 1.2 at%, returning the total oxygen concentration to 2.0 at%. The oxygen concentration added above the background increased approximately linearly with the logarithm of cumulative exposure across both scans, as shown by the red line in Figure 12.

The 300 °C anneal following the time scan led to a 0.1 at% decrease, which was reversed by a 3×10^5 Langmuir exposure. The 500 °C anneal, on the other hand, caused a dramatic 0.6 at% decrease. A total of ~5×10^6 Langmuir left the sample with only 1.7 at% oxygen, compared to the 2.0 at% observed after the the first ~5×10^6 L following the 900 °C reset.

5.3 Oxygen-lithium yo-yo process

Changes in the near surface electronic structure and chemistry across the processing steps applied in the repeated oxygen and lithium deposition experiments are shown in Figure 16. The numerical values are tabulated in Appendix C.

After the **first** 300 °C **cleaning anneal**, the VBM of the oxygen terminated (110)-O was

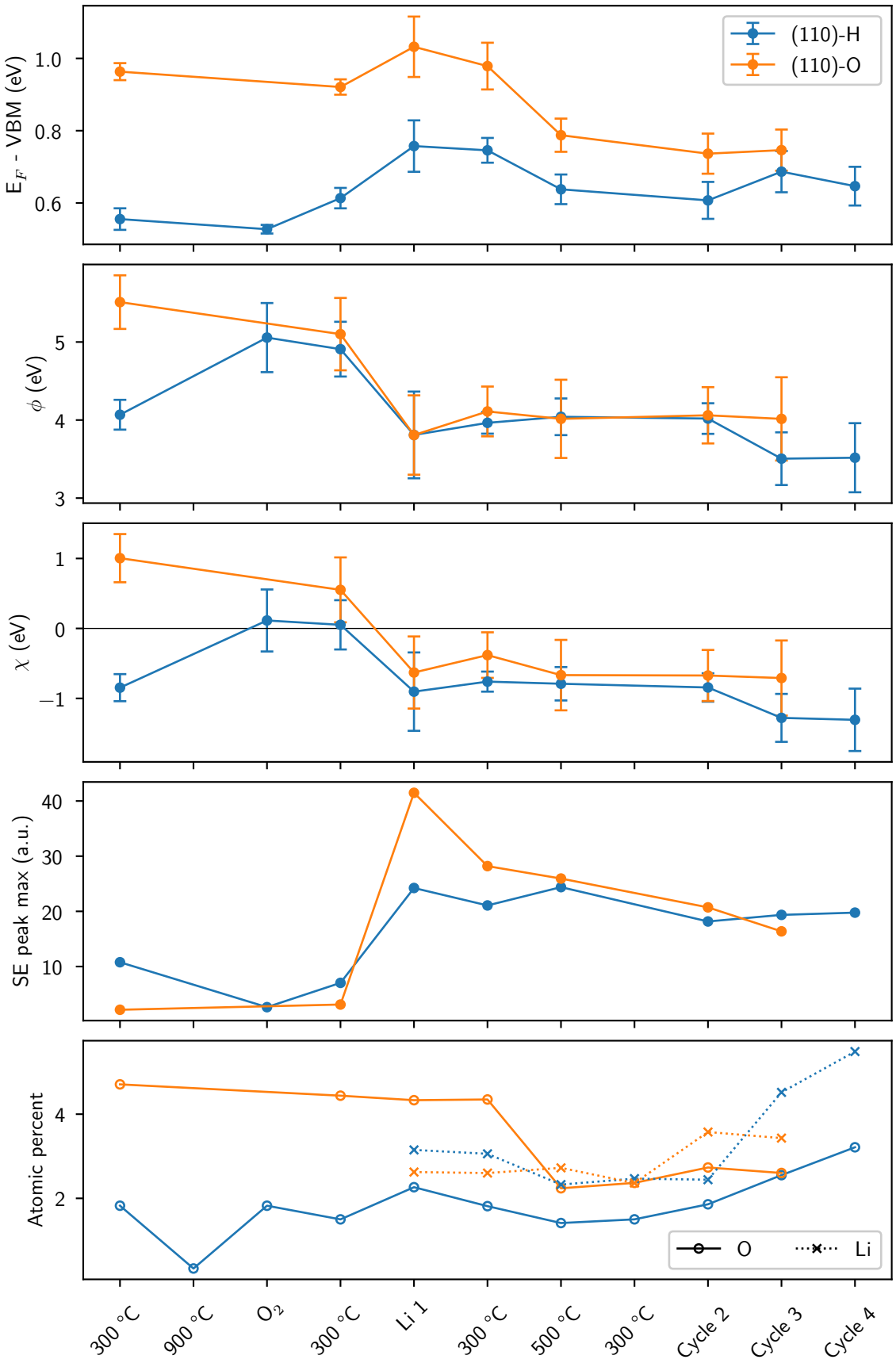

Figure 13: From top to bottom, variation across the processing steps applied in the yo-yo experiment of: VBM relative to the Fermi level, work function, electron affinity, and the maximum of the secondary electron peak from normalised UPS spectra, as well as the atomic concentrations of oxygen and lithium.

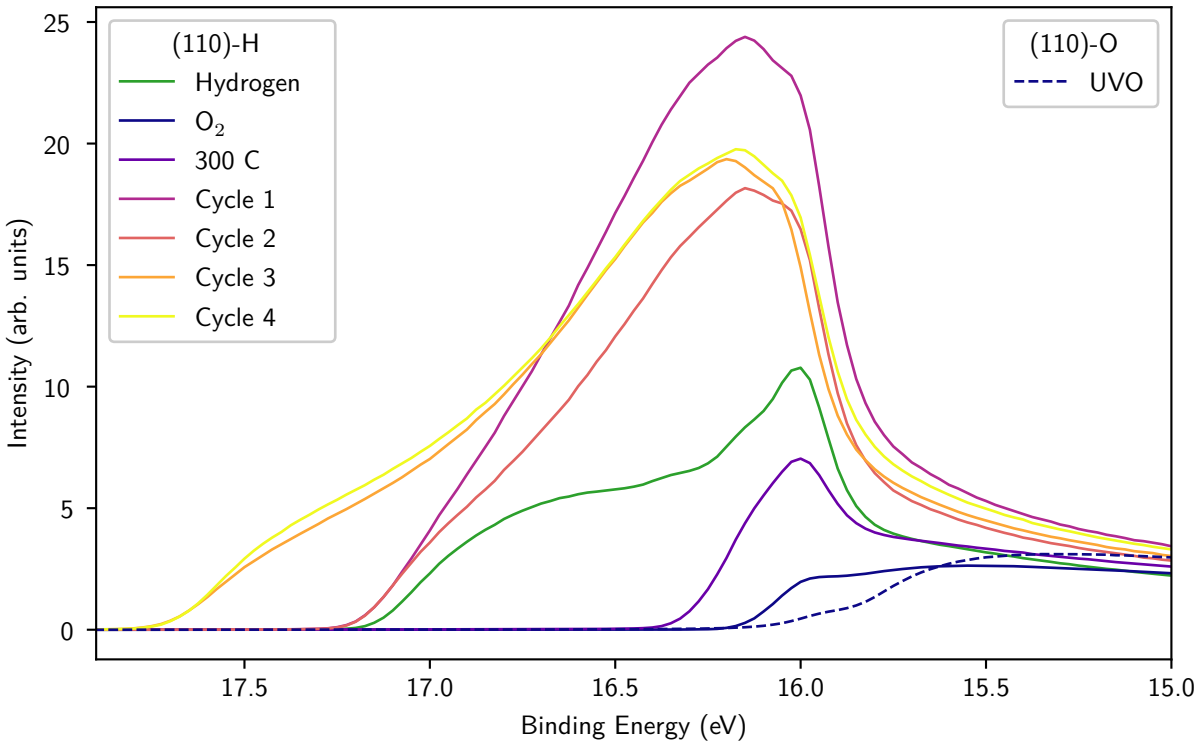

Figure 14: The high binding energy side of the UPS spectrum of the (110)-H sample after various steps in the yo-yo process. Cycle 1 refers to the state of the sample following the 500 °C anneal after the first lithium deposition. The spectrum for the UVO treated surface is shown by a dashed line for comparison.

~0.4 eV further below the Fermi level than that of the hydrogen terminated (110)-H, and the (5.5 ± 0.3) eV work function of the (110)-O was significantly higher than the (4.1 ± 0.2) eV of the (110)-H. Correspondingly, the hydrogen terminated sample showed an NEA of (−0.9 ± 0.2) eV and a characteristic sharp secondary electron peak in the UPS spectrum, while the oxygen terminated sample had a PEA of (1.0 ± 0.3) eV and no sharp peak, as shown in Figure 14. The 4.7 at% oxygen measured on the (110)-H sample is significantly greater than the 3.2 at% observed after the previous UVO treatment, which could be due to contributions from molybdenum oxides as discussed in Section 4.5

Molecular oxygen treatment of the (110)-H sample led to a 1.5 at% increase in the oxygen concentration above the background, greater than the 1.2 at% seen in previous experiments despite the lesser total exposure. This treatment increased the work function to (5.1 ± 0.4) eV, which raised the electron affinity to near zero: (0.1 ± 0.4) eV. The NEA peak in the UPS spectrum was lost after the O_2 treatment and the spectrum to became similar in shape to the UVO treated sample.

The **cleaning anneal** prior to the first lithium deposition (Li 1) decreased the oxygen concentration on both samples by 0.3 at%. Differences in the electronic properties of the (110)-O compared to the first cleaning anneal were partly attributed to measurement of a different area, as noted in Section 4.7. This anneal led to the remergence of a peak in the UPS spectrum of the (110)-H sample (Figure 14), suggesting partial hydrogen termination.

Lithium deposition resulted in lithium concentrations of 2.6 and 3.2 at% for the (110)-O and (110)-H samples respectively. The 0.7 at% increase in oxygen on the (110)-H sample, which was deposited on first, was attributed to lithium oxide from the lithium source, which had not been used for a while. The work function of both samples dropped to (3.8 ± 0.5) eV, accompanied by a ~0.1 eV increase in the difference between the VBM and Fermi energies. The resulting electron affinity of the (110)-H was nominally more negative than the (110)-O sample,

(−0.9 ± 0.6) eV compared to (−0.6 ± 0.5) eV, however the maximum of the secondary electron peak was just over half the relative intensity.

The **post-deposition anneals** caused the observed state of the two samples to become more similar. The lithium and oxygen concentration on (110)-H decreased roughly in parallel. However, for (110)-O, the lithium remained approximately constant while the oxygen concentration decreased precipitously by 2.1 at% during the 500 °C anneal. The VBM became closer to the Fermi level for both samples, although the change was twice as large for (110)-O. This counteracted a slight overall increase in work function, leaving the electron affinity roughly unchanged.

Figure 15 shows **work function maps** for the first cycle. The mean values of these maps follow the work functions found by UPS, but are slightly lower due to the banding at the top and bottom caused by the non-isochromaticity of the energy filter [40]. The O_2 treated sample, (110)-H, was free of major defects, and showed a generally consistent work function across the analysis area. On the other hand, the defects on the UVO treated sample, (110)-O, had a lower work function than the surroundings before lithium deposition, but a higher work function after. However, by the end of the cycle, the 0.04 eV standard deviation of the work function was very similar to the 0.03 eV for (110)-H.

The **second cycle** saw the oxygen concentration increase by 0.36 at% on both samples. The lithium concentration on (110)-H remained roughly the same, while that on (110)-O increased to above the observed oxygen concentration. The secondary electron maximum and E_F - VBM decreased in parallel, while the the work function and electron affinity remained approximately constant for both samples.

During the **third cycle**, the state of the samples diverged. While little change was observed for (110)-O, the oxygen concentration on (110)-H continued to increase, matching that of the initially UVO treated sample. The lithium concentration increased dramatically by 2.1 at%, and the work function dropped by 0.5 eV to (3.5 ± 0.3) eV. Combined with a slight raising of the Fermi level, this led to a more negative electron affinity of (−1.3 ± 0.5) eV.

The **fourth cycle**, conducted on the (110)-H only, led to a further increase in the oxygen concentration to 3.2 at%, the same as observed from the first UVO treatment. The lithium concentration also increased by 1.0 at%, to a final value of 5.5 at%. However, the electronic structure did not change significantly.

As shown in Figure 16, the O 1s peak shifted to lower binding energy over the course of the yo-yo cycles.

6 Discussion

6.1 Hydrogen termination and desorption

The (4.1 ± 0.2) eV work function, and (−0.9 ± 0.2) eV electron affinity observed for the hydrogen terminated sample are in good agreement with the 3.9 eV and −1.0 eV, respectively, reported for the hydrogen terminated (110) surface by Diederich *et al.* [11].

6.1.1 Change in C 1s peak after desorption anneal

The shift and broadening of the C 1s peak, as set out in Section 5.1, is thought not to originate directly from changes in carbon bonding. Carbon-oxygen bonds result in a higher binding energy component, and molybdenum carbide a lower binding energy component, than carbon-carbon bonds [17]. Therefore desorption of oxygen and migration of a molybdenum carbide phase towards the surface would, if anything, cause the C 1s peak to shift to lower binding energy. Carbon-hydrogen bonds lead to a C 1s component at an almost identical binding energy to carbon-carbon, and as such are indistinguishable by XPS.

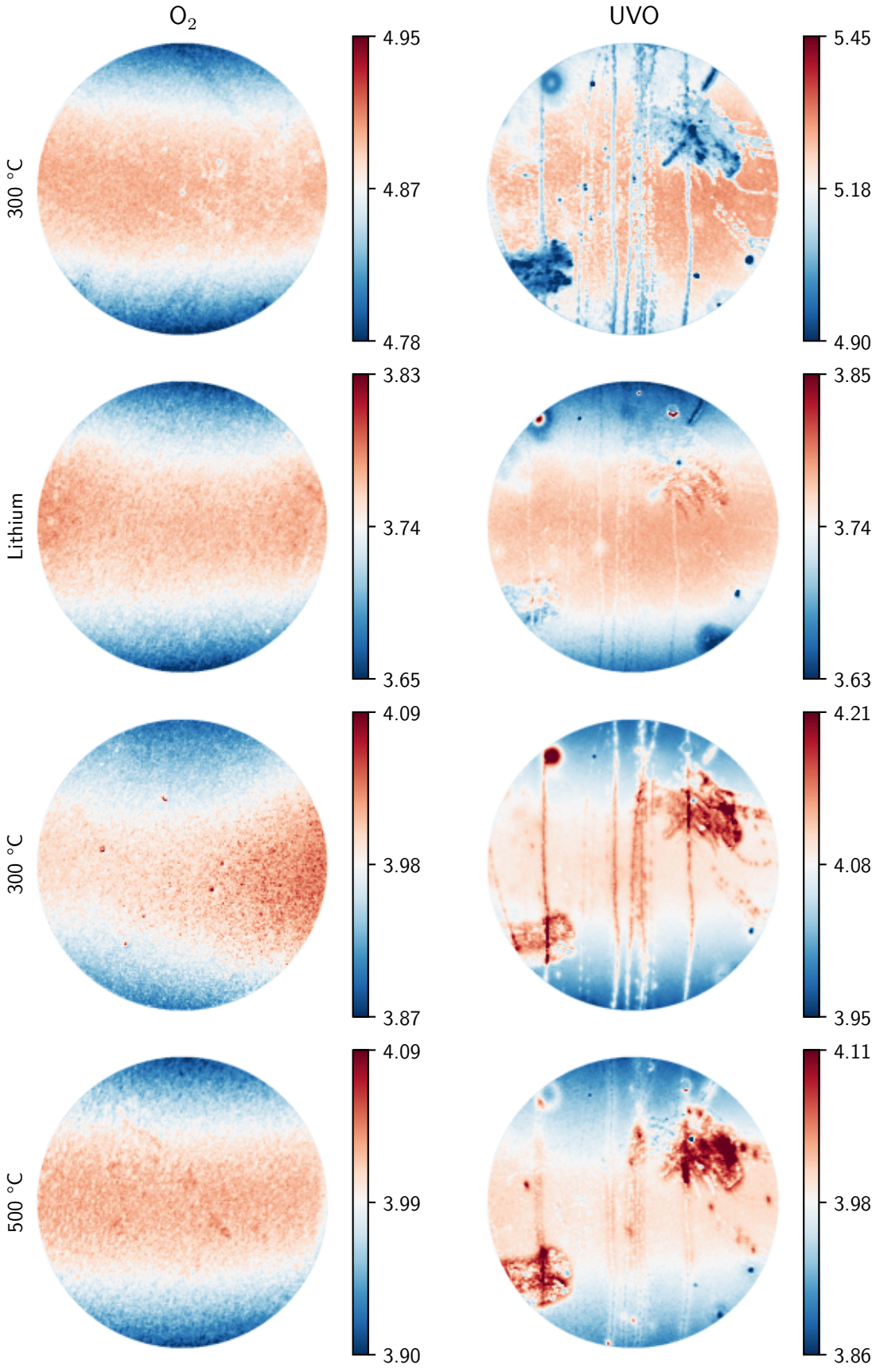

Figure 15: Work function maps of the O_2 (left) and UVO (right) treated samples after a 300 °C cleaning anneal (top), the first lithium deposition, and the subsequent 300 °C and 500 °C anneals (bottom). A 3σ range around the mean is displayed. Values are in eV. Map diameters are (118.3 ± 0.3) µm and (158.5 ± 0.4) µm for the O_2 and UVO treated samples respectively.

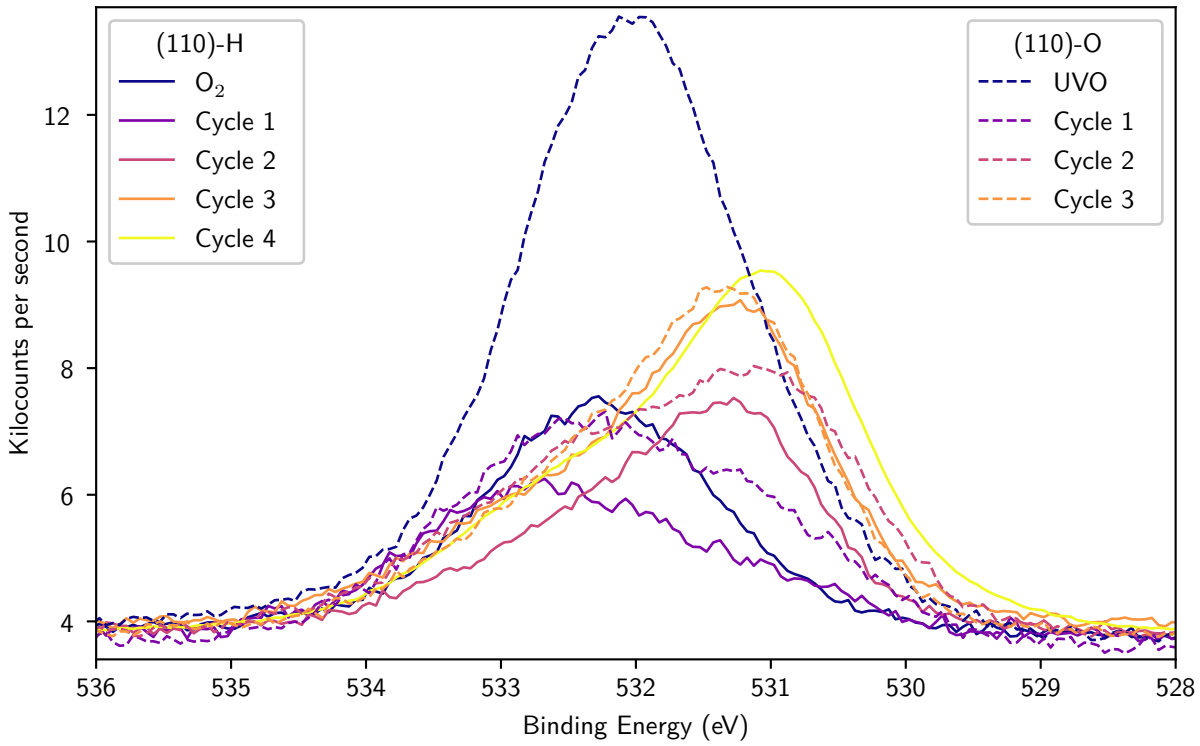

Figure 16: Shift of the O 1s XPS peak to lower binding energy during the yo-yo process. Cycle 1 refers to the state of the samples after the first lithium deposition, followed by 300, 500, and 300 °C anneals.

Wan *et al.* observed the difference in binding energy between the C 1s and O 1s peaks to shift during oxygen termination by cracking, with the C 1s position fixed on the (100) surface, but the O 1s position fixed on the (111) surface [31]. Following DFT simulations this was attributed to the change in surface dipole from the oxygen termination. However, in this work, the change seen after the desorption anneal was much more significant than any subsequent changes during oxygen and lithium deposition, so an explanation based solely on surface dipole changes is discounted.

The shift and broadening is therefore attributed to some quirk of the sample used. Further studies of different samples may be able to confirm this.

6.1.2 Remaining hydrogen termination post desorption anneal

The resurgence of a secondary electron peak following a 300 °C anneal after O_2 exposure, and a corresponding loss of oxygen, suggests that a partial hydrogen termination remains, in agreement with Greenwood [16]. As hydrogen is difficult to pump out of a vacuum system, a relatively high partial pressure is expected to remain in the system after a 900 °C anneal, resulting in re-adsorption of hydrogen onto the cleaned surface. Use of a non-evaporable getter which can efficiently pump hydrogen, as has recently been installed in the NanoESCA system, may enable re-adsorption to be minimised.

6.2 Oxygen termination

6.2.1 UV-ozone treatment

The oxygen concentration of 3.2 at% produced by the UV-ozone treatment is significantly lower than the 5-8 at% reported for the (100) surface [16, 17, 28]. This result is in broad agreement with the observations of Chaudhuri *et al.*, who found that a p(2 × 2)Keto-Ether$_5$ phase,

calculated to have a low coverage of 5.5 atoms/nm^2, was most consistent with their XPS measurements on an acid oxidised (110) surface [26]. This corresponds to a coverage of a quarter of a monolayer on an atomically flat (110) surface, which has a surface dangling bond density of $4/(\sqrt{2} \times 0.35677^2) = 22.2$ atoms/nm^2 at room temperature and pressure [41].

The (5.5 ± 0.3) eV work function and (1.0 ± 0.3) eV electron affinity of the UVO treated sample are lower than reported for the (100) surface [17], as expected for a lower oxygen coverage.

6.2.2 Low pressure molecular oxygen treatment

The oxygen concentration on a (110) surface which had been annealed to high temperature was observed to increase due to exposure to low pressure, room temperature O_2. This agrees with the TPD study of Bobrov *et al.*, who saw desorption of carbon monoxide (CO) after $\leq$144 Langmuir exposure at ~1 × 10^{-7} mbar, but contrast with the findings of Mackey *et al.*, who did not detect desorption of oxygen after exposure at ~1 × 10^{-6} mbar [33]. Furthermore, the roughly linear increase of oxygen concentration with the logarithm of cumulative exposure suggests that saturation was not reached, after ~1 × 10^7 Langmuir. This contradicts the finding of Dontschuk *et al.* that the oxygen concentration saturates after 1 × 10^4 Langmuir. The maximum pressure used by Dontschuk *et al.* was 1 × 10^{-6} mbar, the minimum used in this study, which might suggest that pressure is more important than time and hence interactions between O_2 molecules influence adsorption. However, the continuity of the trend of oxygen increase above the background across the pressure and time scans indicates that this is not the case.

The maximum observed oxygen concentration resulting from the pressure and time scans was 63% of that seen from UV-ozone treatment, only slightly less than the 70% seen by Greenwood after a 1 × 10^{12} Langmuir exposure on the (100) surface [16]. This suggests low pressure O_2 may be as suitable as high pressure for the purposes of oxygen termination, and corroborates Greenwood's suggestion that remaining partial hydrogen termination is the limiting factor.

The (5.1 ± 0.4) eV work function, and (0.1 ± 0.4) eV electron affinity are 93% and 10% of that seen on the UVO treated surface, respectively. The larger difference in the electron affinity is due to the VBM being closer to the Fermi level in the O_2 treated surface. This could be a result of oxygen and hydrogen playing different roles in band bending and fermi level pinning.

6.2.3 Thermal stability of the oxygen terminated (110) surface

The reduction in oxygen concentration seen after annealing is contextualised by a TPD study of the O_2 treated (110) surface by Bobrov *et al.* [34], in which a main CO desorption peak in the 760–890 °C range was attributed to C-O-C bonds . A relatively smaller peak at 275 °C, similar to that observed at 300 °C on the (111) surface, can be attributed to adsorbed O_2. An even less intense peak at 500 °C was seen to emerge after 144 Langmuir, the maximum exposure used. This suggests that the 300 °C anneal resulted in the loss of adsorbed O_2, as desired for a cleaning anneal.

It is possible that the 30% decrease in oxygen concentration following the 500 °C anneal was due to the desorption of -OH groups. These have been calculated to have a lower adsorption energy than oxygen on (100) and (111) surfaces [42], so desorption would be seen at lower temperatures. The dramatic 2 at% drop in oxygen concentration on the UVO treated sample after it was first annealed at 500 °C could support this assessment, as UVO treatment has been observed to produce a significant -OH termination on the (100) surface [17, 16]. However, comparison with the UVO sample is not direct as it was only annealed at 500 °C after lithium deposition.

Alternatively, the fact that the electronic structure did not change significantly could suggest that the loss of oxygen seen at 500 °C was continued desorption of O_2. The adsorption energy for molecular adsorption of O_2 on the boron-doped (110) diamond surface has been predicted to to be relatively high, at ~3.5 eV, compared to ~4.5 eV for dissociative adsorption [43]. O_2 desorption would not account for the small CO TPD peak seen at 500 °C by Bobrov *et*

al., however. Fitting the O 1s XPS peak to determine the relative proportions of bonds before and after anneals may elucidate the matter.

6.3 Oxygen-lithium termination

6.3.1 First lithium deposition and annealing

The 3.8 ± 0.5 eV work function produced by the first lithium deposition was higher than the 2.8 ± 0.1 eV reported by Martin on the (100) surface [14]. The calculated electron affinities of (−0.9 ± 0.6) eV and (−0.6 ± 0.5) eV for the (110)-H and (110)-O samples, respectively, were correspondingly less negative than the −2.1 ± 0.1 eV of Martin. In addition to the different crystal orientation, this is thought to arise from use of a different deposition process.

The 4.0 ± 0.2 eV work function of the (110)-H sample after annealing at 500 °C is also higher, although to a lesser extent, than the values reported by Greenwood for the (100) and (111) surfaces. The deposition method used was the same as detailed here, but with orders of magnitude greater O_2 exposure and double the lithium deposition time [16]. As in this work, Greenwood observed the electron affinity of a UVO treated sample to be closer to zero than that of an O_2 treated sample: −0.95 ± 0.19 vs −1.38 ± 0.31 eV for the (100) surface, as calculated by UPS. However, the difference in that case arose primarily from the work function, whereas here the work functions of the differently oxygen terminated samples were very similar.

That the maximum of the normalised secondary electron peak was greater for the (110)-O sample, with higher electron affinity, is unsurprising, as the secondary electron yield depends on a complex combination of material properties [25]. The 50% reduction in the maximum following the 300 °C anneal is correlated with the emergence of above average work functions at defects seen in the EF-PEEM maps (Figure 15). The same defects were observed to show below average work functions on the oxygen terminated surface prior to lithium deposition. This suggests less, or weaker, bonding of oxygen at defect sites. The presence of similar defects has not previously been observed on UVO treated (100) diamond [17, 16], so could be attributed to the (110) surface. As or more likely a cause is poor sample handling. Surface roughness measurements before and after UVO treatment would clarify this issue.

The 0.5 at% difference in observed lithium concentration between the samples post-deposition can be explained by slight differences in deposition conditions. That the lithium concentration was higher on (110)-H despite lower oxygen concentration supports the suggestion that some lithium oxide was deposited.

6.4 Yo-yo cycles

Figure 13 shows that the work function and E_F - VBM are correlated: generally one increases as the other decreases. This suggests that the surface dipole causes simultaneous lowering of the vacuum level and downward band bending, in contrast with the constant band bending of 0.7 ± 0.2 eV seen by O'Donnel *et al.* on the lithiated (100) surface [15]. The $\pm$0.2 eV uncertainty does, however, cover the observed range in E_F - VBM, which was 0.23 eV for (110)-H and 0.43 eV for (110)-O. The challenges in determining the VBM position using UPS, as previously noted, mean that further investigation, for example with angle-resolved photoelectron spectroscopy (ARPES), would be required to confirm this trend. As the work function is larger than E_F - VBM, and its range of change is greater, it is the dominant influence on the electron affinity.

The shift of the O 1s peak to lower binding energy (Figure 16) is indicative of the formation of O-Li bonds [14, 44, 16]. Despite this shift occurring after the second cycle for both samples, negligible change in the electronic structure was observed. The reason for this is unclear.

The most notable result of the cycling process is the 0.5 eV drop in the work function of (110)-H after the third cycle, and the corresponding 0.4 eV drop in the electron affinity. The cause of this change was an increase in O-Li bonding as seen by the concurrent increase in observed oxygen and lithium concentration, and the further shifting of the O 1s peak. That

the (110)-O did not show this behaviour suggests saturation of C-O-Li bonds was reached. A lower saturation point compared to (110)-H could be explained by the observed defects being unfavourable for such bonding.

The maximum of the (110)-H secondary electron peak remained at approximately the same binding energy after the third cycle, while the high binding energy tail extended. This would seem to validate the assumption of secondary electron scattering into surface states below the CBM, which was noted in Section 2.2.2.

The fourth cycle on (110)-H showed similar behaviour to the second cycle, with an increase in oxygen-lithium bonding causing negligible observable change to the electronic structure. It would be interesting to see if this pattern continues with further cycling.

To the author's knowledge, such a change in the electron affinity on diamond due to repeat processing has only previously been observed by O'Donnel *et al.*, who conducted sequential anneals of an oxygen-lithium terminated (100) surface at increasing temperatures up to 800 °C, and suggested formation of true NEA is an energy activated process [15]. It is possible that the cumulative time annealing at 500 °C was sufficient for such an activation.

7 Conclusion

Exposure to room temperature O_2 at pressures $\leq 1 \times 10^{-2}$ mbar was shown to be a viable method of terminating the diamond (110) surface with oxygen, with the limiting factor determined to be remaining hydrogen termination. Investigation of the thermal stability of the oxygen terminated surface resulted in broad agreement with literature, although more study is needed.

Repeated oxygen exposure, lithium deposition and annealing at 500 °C is found to produce a work function of 3.5 ± 0.3 eV and an electron affinity of −1.3 ± 0.5 eV, lower than achieved by a single cycle. The reasons for this are unclear, but may relate to an activated process as has been suggested in the literature. Comparison with an oxygen terminated surface produced by UV-ozone treatment suggests the presence of defects limits the achievable negative electron affinity.

Many avenues for exploration and improvement are suggested, including using surfaces less contaminated by hydrogen and other foreign species, and conducting a similar study on the more common (100) surface.

Appendices

A Comparison of oxidation methods

Table 3: Comparison of oxidation methods found in literature. Where oxygen content is given as a percentage, this is an atomic percentage calculated from XPS measurements.

Method	Surface	O content	Details	Ref.
Acid oxidation	(100)	10.4%	KNO_3 with H_2SO_4, C – OH dominant	[17]
	(100)	4.8-5.3%	Various solutions	[28]
	DP, PCD	7-9%	Various solutions, C – OH dominant	[30]
	(100)	10.2%	HNO_3 with H_2SO_4	[29]
	(100)	5-15.5%	$HClO_4$:H_2SO_4:HNO_3 (1:3:4), ARXPS polar angles 0 to 84.6°, formation of sp^2 C during oxidation	[27]
	(110)		500 °C anneal, only 2 peak components	[26]
UV-ozone	(100)	7.6%	Majority C – O – C	[17]
	(100)	7.1 ± 0.3%		[28]
	(100)	6.8 ± 0.4%		[28]
	(100)	5.5%	500 mbar in vacuum	[29]
	(100)	6.8%	In atmosphere	[29]
	(100)	5.3%	Primarily C – OH, then C = O, then C – O – C	[16]
cracking	(100)	4.3%	Cracking produced up to 60% atomic O, large majority C – O – C	[17]
	(100)	~6.5%	No saturation after 130 min, only ratio of O 1s and C 1s areas given	[31]
	(111)	~7.0%	as above	[31]
	(100)		TPD, desorption as CO at ~600 °C	[45]
O_2	(100)	None	Hydrogenated surface, room temperature	[32]
O_2*	(100)	1 ML	700 kL, assumed negligible cracking, observed roughening	[32]
O_2	(110)	None	TPD and AES, hydrogen-free, room temperature	[33]
O_2*	(110)	Saturated	TPD, saturation of room temperature surface after 2400 L, etching of low temperature adsorption sites when surface 625 °C	[33]
O_2	(110)		TPD, single CO desorption between 760 and 890 °C for exposures up to 144 L, suggested C – O – C only	[34]
O_2	(111)		TPD, two CO desorption peaks at around 790 and 1030 °C for exposures up to 15 L	[34]
O_2	(100)	Saturated	Hydrogen free, saturation after 1×10^4 L, no substantial changes after 450 °C, 60% desorption after 700 °C	[46]
O_2	(100)	3.7%	1.5 bar for 20 minutes, primarily C – OH, then C = O, then C – O – C	[16]
O_2	(111)	1.5%	as above	[16]
ALD	(100)	6.7 ± 0.4%		[28]
O_2 plasma	(100)	7.4%	mostly C-O-C, then C-OH, then C=0	[17]

B Diamond substrate properties

Table 4: Specifications, tolerances, and material properties of the undoped, (110) oriented, single crystal diamond from Element Six [47].

SKU	145-500-0573
Carat Weight EA	0.10 ct
Crystallographic Orientation (Miscut)	+/-3°
Crystallography	Typically 100% single sector {100}
Lateral Dimensions Measured	to smaller side
Edges	Laser Cut
Edge Features	< 0.2 mm
Edge Orientation	<100> edges & <110>
Face Orientation	{110} faces
Laser Kerf	3°
Lateral Tolerance	+0.2/-0 mm
Length	6.80 mm <100>
Side 1, Roughness, Ra	polished, Ra < 30 nm
Side 2, Roughness, Ra	polished, Ra < 30 nm
Thickness Tolerance	+0.01/-0.02 mm
Thickness Dimension	0.2 mm
Width	3.30 mm <100>
Boron Concentration [B]	<0.05 ppm
Nitrogen Concentration	< 1 ppm

C Table of numerical results for the yo-yo process

Table 5: Numerical results from XPS and UPS studies of the yo-yo process.

Step	Sample	C 1s (at%)	O 1s (at%)	Li 1s (at%)	SECO (eV)	VBM (eV)	ϕ (eV)	χ (eV)	SE Max. (arb.)
300 °C	(110)-H	98.17	1.83		17.15±0.19	0.555±0.030	4.07±0.19	-0.85±0.19	10.8
	(110)-O	95.29	4.71		15.71±0.34	0.963±0.024	5.51±0.34	1.00±0.34	2.2
900 °C	(110)-H	99.67	0.33						
O_2	(110)-H	98.18	1.82		16.16±0.44	0.527±0.012	5.06±0.44	0.11±0.44	2.6
300 °C	(110)-H	98.50	1.50		16.31±0.35	0.613±0.028	4.91±0.35	0.05±0.35	7
	(110)-O	95.56	4.44		16.12±0.46	0.921±0.021	5.10±0.46	0.55±0.46	3.1
Li 1	(110)-H	94.58	2.26	3.15	17.41±0.56	0.757±0.071	3.81±0.56	-0.90±0.56	24.2
	(110)-O	93.04	4.33	2.62	17.41±0.51	1.032±0.084	3.81±0.51	-0.63±0.52	41.5
300 °C	(110)-H	95.13	1.81	3.06	17.25±0.14	0.746±0.034	3.96±0.14	-0.76±0.14	21.1
	(110)-O	93.05	4.35	2.6	17.11±0.32	0.979±0.065	4.11±0.32	-0.38±0.33	28.2
500 °C	(110)-H	96.26	1.41	2.33	17.18±0.23	0.638±0.041	4.04±0.23	-0.79±0.24	24.4
	(110)-O	95.04	2.24	2.72	17.20±0.50	0.788±0.046	4.02±0.50	-0.67±0.50	25.9
300 °C	(110)-H	96.03	1.50	2.47					
	(110)-O	95.27	2.37	2.36					
Cycle 2	(110)-H	95.70	1.86	2.44	17.20±0.20	0.607±0.051	4.02±0.20	-0.84±0.20	18.2
	(110)-O	93.69	2.73	3.58	17.16±0.36	0.736±0.056	4.06±0.36	-0.67±0.36	20.7
Cycle 3	(110)-H	92.93	2.55	4.52	17.71±0.34	0.687±0.057	3.51±0.34	-1.28±0.34	19.4
	(110)-O	93.97	2.60	3.43	17.20±0.53	0.746±0.057	4.01±0.53	-0.71±0.54	16.4
Cycle 4	(110)-H	91.30	3.21	5.49	17.70±0.44	0.647±0.054	3.52±0.44	-1.31±0.45	19.8

D Sample handling advice to students about to undertake a similar project

- Take care preparing clean samples
- Keep samples the right way up: mark with the laser before BDD growth
- Just use 2 samples at a time - lots easier to deal with and you can get more done
- For sample holders, make sure to use a flat foil with a window as large as possible.
- If possible, use samples bigger than 3 by 3 mm
- Practice using tweezers in stressful situations

Certification of ownership of the copyright

This Project Report is presented as part of, and in accordance with, the requirements for the degree of MSci at the University of Bristol, Faculty of Science and Engineering.

I hereby assert that I own exclusive copyright in the item named below. I give permission to the University of Bristol Library to add this item to its stock and to make it available for consultation in the library, and for inter-library lending for use in another library. I also give consent for this report to made available electronically to staff and students within the University of Bristol. It may be copied in full or in part for any bona fide library or research work. No quotation and no information derived from it may be published without the author's prior consent.

Author	Callum Jeffrey Brown
Title	Enhancement of negative electron affinity on the diamond (110) surface by cyclic low pressure molecular oxygen treatment and lithium deposition
Date of submission	2025-03-20

I agree that submission of this report constitutes signing of this declaration.

This project report is the property of the University of Bristol and may only be used with due regard to the rights of the author. Bibliographical references may be noted, but no part may be copied for use or quotation in any published work without the prior permission of the author. In addition, due acknowledgement for any use must be made.

References

[1] Michael C. James et al. 'A review of surface functionalisation of diamond for thermionic emission applications'. en. In: *Carbon* 171 (Jan. 2021), pp. 532–550. ISSN: 00086223. DOI: 10.1016/j.carbon.2020.09.019. URL: https://linkinghub.elsevier.com/retrieve/pii/S0008622320308678 (visited on 02/09/2024).

[2] R.J. Nemanich et al. 'Negative electron affinity surfaces of aluminum nitride and diamond'. en. In: *Diamond and Related Materials* 5.6-8 (May 1996), pp. 790–796. ISSN: 09259635. DOI: 10.1016/0925-9635(95)00485-8. URL: https://linkinghub.elsevier.com/retrieve/pii/0925963595004858 (visited on 18/03/2025).

[3] Kian Ping Loh et al. 'Negative electron affinity of cubic boron nitride'. en. In: *Diamond and Related Materials* 8.2-5 (Mar. 1999), pp. 781–784. ISSN: 09259635. DOI: 10.1016/S0925-9635(98)00293-3. URL: https://linkinghub.elsevier.com/retrieve/pii/S0925963598002933 (visited on 18/03/2025).

[4] Lu Cheng et al. 'Bandgap evolution of diamond'. en. In: *Diamond and Related Materials* 132 (Feb. 2023), p. 109638. ISSN: 09259635. DOI: 10.1016/j.diamond.2022.109638. URL: https://linkinghub.elsevier.com/retrieve/pii/S0925963522008202 (visited on 18/03/2025).

[5] Ramiz Zulkharnay. 'Electron Emission Studies of Scandium on Diamond for Thermionic Solar Energy Generation Devices'. en. PhD. University of Bristol, 2023.

[6] Kane M. O'Donnell et al. 'Direct observation of phonon emission from hot electrons: spectral features in diamond secondary electron emission'. en. In: *Journal of Physics: Condensed Matter* 26.39 (Sept. 2014). Number: 39 Publisher: IOP Publishing, p. 395008. ISSN: 0953-8984. DOI: 10.1088/0953-8984/26/39/395008. URL: https://dx.doi.org/10.1088/0953-8984/26/39/395008 (visited on 30/12/2024).

[7] Corey Melnick and Massoud Kaviany. 'From thermoelectricity to phonoelectricity'. en. In: *Applied Physics Reviews* 6.2 (June 2019). Number: 2, p. 021305. ISSN: 1931-9401. DOI: 10.1063/1.5031425. URL: https://pubs.aip.org/aip/apr/article/570297 (visited on 10/09/2024).

[8] Neil A. Fox. 'Low Pressure Synthesis of Diamond by Chemical Vapour Deposition and Its Technological Applications'. en. In: *Elemental Carbon*. Ed. by Peter J F Harris. Royal Society of Chemistry, Dec. 2024, pp. 301–351. ISBN: 978-1-83916-451-4 978-1-83916-999-1 978-1-83916-998-4. DOI: 10.1039/9781839169984-00301. URL: https://books.rsc.org/books/book/2247/chapter/8277029/Low-Pressure-Synthesis-of-Diamond-by-Chemical (visited on 14/02/2025).

[9] F. Maier, J. Ristein and L. Ley. 'Electron affinity of plasma-hydrogenated and chemically oxidized diamond (100) surfaces'. en. In: *Physical Review B* 64.16 (Oct. 2001), p. 165411. ISSN: 0163-1829, 1095-3795. DOI: 10.1103/PhysRevB.64.165411. URL: https://link.aps.org/doi/10.1103/PhysRevB.64.165411 (visited on 13/03/2025).

[10] J. B. Cui, J. Ristein and L. Ley. 'Electron Affinity of the Bare and Hydrogen Covered Single Crystal Diamond (111) Surface'. en. In: *Physical Review Letters* 81.2 (July 1998), pp. 429–432. ISSN: 0031-9007, 1079-7114. DOI: 10.1103/PhysRevLett.81.429. URL: https://link.aps.org/doi/10.1103/PhysRevLett.81.429 (visited on 18/03/2025).

[11] L Diederich et al. 'Electron emission and NEA from differently terminated, doped and oriented diamond surfaces'. en. In: *Diamond and Related Materials* 8.2-5 (Mar. 1999). Number: 2-5, pp. 743–747. ISSN: 09259635. DOI: 10.1016/S0925-9635(98)00339-2. URL: https://linkinghub.elsevier.com/retrieve/pii/S0925963598003392 (visited on 22/10/2024).

[12] Kane M. O'Donnell, Tomas L. Martin and Neil L. Allan. 'Light Metals on Oxygen-Terminated Diamond (100): Structure and Electronic Properties'. en. In: *Chemistry of Materials* 27.4 (Feb. 2015). Number: 4, pp. 1306–1315. ISSN: 0897-4756, 1520-5002. DOI: 10.1021/cm5043155. URL: https://pubs.acs.org/doi/10.1021/cm5043155 (visited on 14/10/2024).

[13] Ramiz Zulkharnay, Neil L. Allan and Paul W. May. 'Ab initio study of negative electron affinity on the scandium-terminated diamond (100) surface for electron emission devices'. en. In: *Carbon* 196 (Aug. 2022), pp. 176–185. ISSN: 00086223. DOI: 10.1016/j.carbon.2022.04.067. URL: https://linkinghub.elsevier.com/retrieve/pii/S0008622322003451 (visited on 22/10/2024).

[14] Tomas Liam Martin. 'Lithium oxygen termination as a negative electron affinity surface on diamond: a computational and photoemission study'. English. PhD. University of Bristol, Nov. 2011. URL: https://research-information.bris.ac.uk/en/studentTheses/lithium-oxygen-termination-as-a-negative-electron-affinity-surfac.

[15] Kane M. O'Donnell et al. 'Diamond Surfaces with Air Stable Negative Electron Affinity and Giant Electron Yield Enhancement'. en. In: *Advanced Functional Materials* 23.45 (Dec. 2013). Number: 45, pp. 5608–5614. ISSN: 1616-301X, 1616-3028. DOI: 10.1002/adfm.201301424. URL: https://onlinelibrary.wiley.com/doi/10.1002/adfm.201301424 (visited on 07/11/2024).

[16] William Greenwood. 'A New Oxygen And Lithium Diamond Termination For Optimised Graphene Electronics'. MSci. University of Bristol, 2024.

[17] Ramiz Zulkharnay, Gulnur Zulpukarova and Paul W. May. 'Oxygen-terminated diamond: insights into the correlation between surface oxygen configurations and work function values'. en. In: *Applied Surface Science* 658 (June 2024), p. 159776. ISSN: 01694332. DOI: 10.1016/j.apsusc.2024.159776. URL: https://linkinghub.elsevier.com/retrieve/pii/S0169433224004896 (visited on 10/10/2024).

[18] R. L. Bell. *Negative Electron Affinity Devices*. Clarendon Press, 1973.

[19] Masahiro Kashima et al. 'The photoemission characteristics of a NEA InGaN photocathode by simultaneously supplying Cs and O2'. en. In: *Applied Surface Science* 599 (Oct. 2022), p. 153882. ISSN: 01694332. DOI: 10.1016/j.apsusc.2022.153882. URL: https://linkinghub.elsevier.com/retrieve/pii/S0169433222014258 (visited on 10/10/2024).

[20] Andrew Zangwill. *Physics at surfaces*. English. Section: xiii, 454 pages : illustrations ; 24 cm. Cambridge [Cambridgeshire]: Cambridge University Press, 1988. ISBN: 0-521-32147-6 978-0-521-32147-1 0-521-34752-1 978-0-521-34752-5.

[21] Kane M. O'Donnell et al. 'Photoelectron emission from lithiated diamond'. en. In: *physica status solidi (a)* 211.10 (2014). Number: 10 _eprint: https://onlinelibrary.wiley.com/doi/pdf/10.1002/pssa pp. 2209–2222. ISSN: 1862-6319. DOI: 10.1002/pssa.201431414. URL: https://onlinelibrary.wiley.com/doi/abs/10.1002/pssa.201431414 (visited on 30/12/2024).

[22] Fred A. Stevie and Carrie L. Donley. 'Introduction to x-ray photoelectron spectroscopy'. en. In: *Journal of Vacuum Science & Technology A: Vacuum, Surfaces, and Films* 38.6 (Dec. 2020). Number: 6, p. 063204. ISSN: 0734-2101, 1520-8559. DOI: 10.1116/6.0000412. URL: https://pubs.aip.org/jva/article/38/6/063204/1024200/Introduction-to-x-ray-photoelectron-spectroscopy (visited on 08/09/2024).

[23] James E. Whitten. 'Ultraviolet photoelectron spectroscopy: Practical aspects and best practices'. en. In: *Applied Surface Science Advances* 13 (Feb. 2023), p. 100384. ISSN: 26665239. DOI: 10.1016/j.apsadv.2023.100384. URL: https://linkinghub.elsevier.com/retrieve/pii/S2666523923000193 (visited on 15/02/2025).

[24] S. Prawer et al. 'Spatial extent of band bending in diamond due to ion impact as measured by secondary electron emission: Experiment and theory'. en. In: *Physical Review B* 73.15 (Apr. 2006), p. 153202. ISSN: 1098-0121, 1550-235X. DOI: 10.1103/PhysRevB.73.153202. URL: https://link.aps.org/doi/10.1103/PhysRevB.73.153202 (visited on 19/03/2025).

[25] J.E. Yater and A. Shih. 'Characterization of Secondary Electron Emission from Materials with Low or Negative Electron Affinity'. en. In: *MRS Proceedings* 509 (1998), p. 125. ISSN: 0272-9172, 1946-4274. DOI: 10.1557/PROC-509-125. URL: http://link.springer.com/10.1557/PROC-509-125 (visited on 20/03/2025).

[26] Shayantan Chaudhuri et al. 'Coexistence of carbonyl and ether groups on oxygen-terminated (110)-oriented diamond surfaces'. en. In: *Communications Materials* 3.1 (Jan. 2022). Number: 1, p. 6. ISSN: 2662-4443. DOI: 10.1038/s43246-022-00228-4. URL: https://www.nature.com/articles/s43246-022-00228-4 (visited on 15/01/2025).

[27] Gonzalo Alba et al. 'Surface States of (100) O-Terminated Diamond: Towards Other 1 × 1:O Reconstruction Models'. en. In: *Nanomaterials* 10.6 (June 2020). Number: 6, p. 1193. ISSN: 2079-4991. DOI: 10.3390/nano10061193. URL: https://www.mdpi.com/2079-4991/10/6/1193 (visited on 31/10/2024).

[28] Ricardo Vidrio et al. 'XPS analysis of molecular contamination and sp^2 amorphous carbon on oxidized (100) diamond'. In: *Materials for Quantum Technology* 4.2 (June 2024). Number: 2, p. 025201. ISSN: 2633-4356. DOI: 10.1088/2633-4356/ad4e8a. URL: https://iopscience.iop.org/article/10.1088/2633-4356/ad4e8a (visited on 31/10/2024).

[29] Javier Navas et al. 'Oxygen termination of homoepitaxial diamond surface by ozone and chemical methods: An experimental and theoretical perspective'. en. In: *Applied Surface Science* 433 (Mar. 2018), pp. 408–418. ISSN: 01694332. DOI: 10.1016/j.apsusc.2017.10.065. URL: https://linkinghub.elsevier.com/retrieve/pii/S0169433217329987 (visited on 12/01/2025).

[30] Chenxi Li et al. 'Systematic comparison of various oxidation treatments on diamond surface'. en. In: *Carbon* 182 (Sept. 2021), pp. 725–734. ISSN: 00086223. DOI: 10.1016/j.carbon.2021.06.050. URL: https://linkinghub.elsevier.com/retrieve/pii/S0008622321006370 (visited on 12/01/2025).

[31] Gary Wan, Mattia Cattelan and Neil A. Fox. 'Electronic Structure Tunability of Diamonds by Surface Functionalization'. en. In: *The Journal of Physical Chemistry C* 123.7 (Feb. 2019). Number: 7, pp. 4168–4177. ISSN: 1932-7447, 1932-7455. DOI: 10.1021/acs.jpcc.8b11232. URL: https://pubs.acs.org/doi/10.1021/acs.jpcc.8b11232 (visited on 10/09/2024).

[32] Pehr E Pehrsson and Thomas W Mercer. 'Oxidation of the hydrogenated diamond (100) surface'. en. In: *Surface Science* 460.1-3 (July 2000). Number: 1-3, pp. 49–66. ISSN: 00396028. DOI: 10.1016/S0039-6028(00)00494-5. URL: https://linkinghub.elsevier.com/retrieve/pii/S0039602800004945 (visited on 11/01/2025).

[33] Bob L. Mackey et al. 'Oxygen Adsorption on the (110)-Oriented Diamond Surface'. en. In: *The Journal of Physical Chemistry B* 105.18 (May 2001). Number: 18, pp. 3803–3812. ISSN: 1520-6106, 1520-5207. DOI: 10.1021/jp003586k. URL: https://pubs.acs.org/doi/10.1021/jp003586k (visited on 12/11/2024).

[34] K Bobrov et al. 'Molecular oxygen adsorption and desorption from single crystal diamond (1 1 1) and (1 1 0) surfaces'. en. In: *Applied Surface Science* 196.1-4 (Aug. 2002). Number: 1-4, pp. 173–180. ISSN: 01694332. DOI: 10.1016/S0169-4332(02)00053-3. URL: https://linkinghub.elsevier.com/retrieve/pii/S0169433202000533 (visited on 12/11/2024).

[35] Edmund Jack William Smith. ‘Growing Diamond on Unusual Substrates’. en. PhD. University of Bristol, Jan. 2022.

[36] Thomas W. Mercer, John N. Russell and Pehr E. Pehrsson. ‘The effect of a hydrogen plasma on the diamond (110) surface’. en. In: *Surface Science* 392.1-3 (Dec. 1997). Number: 1-3, pp. L21–L26. ISSN: 00396028. DOI: 10.1016/S0039-6028(97)00680-8. URL: https://linkinghub.elsevier.com/retrieve/pii/S0039602897006808 (visited on 12/01/2025).

[37] John F. Moulder et al. *Handbook of X-ray Photoelectron Spectroscopy*. Perkin-Elmer Corporation, 1992. ISBN: 0-9627026-2-5.

[38] S. P. Grabowski et al. ‘Electron affinity of AlxGa1−xN(0001) surfaces’. en. In: *Applied Physics Letters* 78.17 (Apr. 2001), pp. 2503–2505. ISSN: 0003-6951, 1077-3118. DOI: 10.1063/1.1367275. URL: https://pubs.aip.org/apl/article/78/17/2503/516889/Electron-affinity-of-AlxGa1-xN-0001-surfaces (visited on 20/03/2025).

[39] Julian Andreas Hochhaus. *Imfitxps*. Programmers: _:n596. Dec. 2024. DOI: 10.5281/ZENODO.8181378. URL: https://zenodo.org/doi/10.5281/zenodo.8181378 (visited on 16/01/2025).

[40] Marten Christopher Patt. *Bulk and surface sensitive energy-filtered photoemission microscopy using synchrotron radiation for the study of resistive switching memories*. eng. Schriften des Forschungszentrums Jülich Reihe Schlüsseltechnologien Band 122. Jülich: Forschungszentrum Jülich, 2016. ISBN: 978-3-95806-130-9.

[41] Argonne National Laboratory. *Lattice Constants*. Jan. 2025. URL: https://7id.xray.aps.anl.gov/calculators/crystal_lattice_parameters.html (visited on 16/01/2025).

[42] D. Petrini and K. Larsson. ‘Theoretical Study of the Thermodynamic and Kinetic Aspects of Terminated (111) Diamond Surfaces’. en. In: *The Journal of Physical Chemistry C* 112.8 (Feb. 2008), pp. 3018–3026. ISSN: 1932-7447, 1932-7455. DOI: 10.1021/jp709625a. URL: https://pubs.acs.org/doi/10.1021/jp709625a (visited on 19/03/2025).

[43] Stefanos Giaremis and Maria Clelia Righi. ‘Tuning the adsorption of H2O, H2 and O2 molecules on diamond surfaces by B-doping’. en. In: *Surfaces and Interfaces* 46 (Mar. 2024), p. 104105. ISSN: 24680230. DOI: 10.1016/j.surfin.2024.104105. URL: https://linkinghub.elsevier.com/retrieve/pii/S2468023024002645 (visited on 12/11/2024).

[44] Sami Ullah et al. ‘An investigation into the surface termination and near-surface bulk doping of oxygen-terminated diamond with lithium at various annealing temperatures’. In: *MRS Advances* 6.12 (Apr. 2021). Number: 12, pp. 311–320. ISSN: 2059-8521. DOI: 10.1557/s43580-021-00060-x.

[45] R. E. Thomas, R. A. Rudder and R. J. Markunas. ‘Thermal desorption from hydrogenated and oxygenated diamond (100) surfaces’. en. In: *Journal of Vacuum Science & Technology A: Vacuum, Surfaces, and Films* 10.4 (July 1992). Number: 4, pp. 2451–2457. ISSN: 0734-2101, 1520-8559. DOI: 10.1116/1.577983. URL: https://pubs.aip.org/jva/article/10/4/2451/464780/Thermal-desorption-from-hydrogenated-and (visited on 19/11/2024).

[46] N Dontschuk et al. ‘X-ray quantification of oxygen groups on diamond surfaces for quantum applications’. en. In: *Materials for Quantum Technology* 3.4 (Dec. 2023), p. 045901. ISSN: 2633-4356. DOI: 10.1088/2633-4356/ad001b. URL: https://iopscience.iop.org/article/10.1088/2633-4356/ad001b (visited on 11/03/2025).

[47] Element Six. *SC110 Plate CVD 6.8x3.3mm, 0.2mm thick P2*. en. Oct. 2024. URL: https://e6cvd.com/us/application/all/sc-6-8x3-3x0-2mm-p2.html (visited on 17/10/2024).